Climate-Driven Risk of Extreme Wildfire in California

Patrick T. Brown[1,2,3,4]*, Holt Hanley[2,4,5], Ankur Mahesh[6], Colorado Reed[7], Scott J. Strenfel[8], Steven J. Davis[9], Adam K. Kochanski[2,4], Craig B. Clements[2,4]

Affiliations:

[1]Breakthrough Institute, Oakland, California

[2]Wildfire Interdisciplinary Research Center (WIRC), San José State University

[3]Energy Policy and Climate Program, Johns Hopkins University

[4]Department of Meteorology and Climate Science, San José State University

[5]KSBW News, Salinas, California

[6]Earth and Planetary Science, University of California Berkeley

[7]Electrical Engineering and Computer Sciences, University of California Berkeley

[8]Pacific Gas and Electric Company, San Francisco, California

[9]Department of Earth System Science, University of California, Irvine

*Corresponding author. Email: Patrick@thebreakthrough.org

Abstract: California has experienced increased instances of extreme wildfire behavior in recent years, but the extent to which this is due to anthropogenic warming has been difficult to determine. Here we quantify empirical relationships between temperature and the risk of extreme daily wildfire growth (>10,000 acres) in California and use these relationships to estimate how extreme growth risk is changing under anthropogenic warming. We subject fires from 2003 to 2020 to differing background climatological temperatures and aridity metrics and find that the fraction of the risk of extreme daily growth attributable to anthropogenic warming to date averages 19% but varies substantially depending on whether background warming pushed fires over critical aridity thresholds. When the historical fires from 2003 to 2020 are subjected to projected end-of-century temperatures, the expected frequency of extreme daily growth events increases by 59% under an emissions scenario in line with the Paris Agreement, compared to an increase of 172% under a very high emissions scenario.

One-Sentence Summary: Analysis of historical data reveal robust relationships between anthropogenic warming and the risk of extreme wildfire behavior in California

California has experienced enhanced extreme wildfire behavior in recent years (*1*-*3*), leading to high-profile catastrophic impacts (*4*, *5*). It is widely accepted that some portion of the change in wildfire behavior is attributable to human-caused warming, but formally quantifying this contribution is difficult due to confounding factors like changes in human population distribution, fuel breaks, ignition patterns, firefighting tactics, forest management strategies, and long-term buildup of fuels (*6*, *7*).

Despite this complexity, in principle, it should be possible to use known physics represented in mechanistic models (*8*) to quantify the contribution of anthropogenic warming to changes in wildfire behavior. However, the tools typically used for the attribution of extreme weather and climate events to anthropogenic warming are global climate models (GCMs) that do not directly simulate wildfires because the wildfire spatial scale is smaller than the grid scale of the typical model. Furthermore, GCMs struggle with the simulation of high spatiotemporal resolution phenomena like daily weather extremes that have an outsized effect on wildfire behavior (*9*).

Thus, most studies on the influence of anthropogenic warming on wildfire activity investigate the relationship indirectly by focusing on how conditions conducive to wildfires are changing over regional and seasonal-mean timescales (*10*-*17*). Studies often make use of a fire-weather or fire-danger index, which has the relationship between temperature and conduciveness to wildfires presupposed.

Here, our goal is to assess anthropogenic warming's influence on the risk of extreme wildfire behavior in California using an empirical approach where the relationship between temperature and risk is learned from the data. We also seek to make attribution statements at the level of individual fires.

Rather than presupposing a specific statistical or functional relationship between temperature and wildfire behavior, we build on recent work (*18*-*21*) and use neural networks and random forests to learn the potentially nonlinear relationship between temperature and wildfire behavior in ways that are highly conditional on the state of other environmental variables. Extreme wildfire behavior can be defined in several ways (*22*), but here we define it as an exceptionally high rate of spread, and in particular, growth of 10,000 acres (about 2/3^{rds} the size of Manhattan) or more in a single day. We focus on these types of occurrences because they have been disproportionately responsible for the exponential increase in observed annual area-burned (*1*, *2*), and they are particularly challenging from a firefighting perspective, which increases the likelihood of loss of life and property.

Our approach can be summarized in two steps: 1) We train an ensemble of machine learning models to learn relationships between environmental conditions (predictors) and the risk of extreme daily fire growth (response), given an active fire (Fig. 1A). 2) We then alter the predictors based on global climate model simulations of future warming, and recalculate risk (Fig. 1D). Thus, we are holding everything about historical conditions during fire-days constant (i.e., ignitions, winds, precipitation, and absolute moisture content of the atmosphere) except for the background climatological temperature. This approach, similar to the "pseudo-global warming" (*23*) or "storyline" approaches (*24*, *25*) of the extreme event attribution literature (*26*), allows us to investigate warming's influence on risk at the granularity of individual days for historical fires.

It is already well-established that temperature's influence on wildfire behavior is not primarily via temperature per se (*27*), but rather through temperature's influence on aridity (*11*, *12*, *28*). Thus, we also propagate changes in temperature into the three other predictor variables that have a direct relationship with temperature (Fig. 1C). These variables are vapor pressure deficit and the two calculated dead-fuel moisture variables (100 hour and 1,000 hour, see Material and Methods).

The central result of this study compares the calculated risks under preindustrial conditions and the calculated risks under warmed conditions using the probability ratio (*29*) (Fig. 1F). For historical extreme growth events, we also calculate the fraction of the risk of that event occurring that can be attributed to anthropogenic warming (*30*) (Fig. 1G). See Materials and Methods as well as a video description of the method: https://youtu.be/lHztGWzghRI)

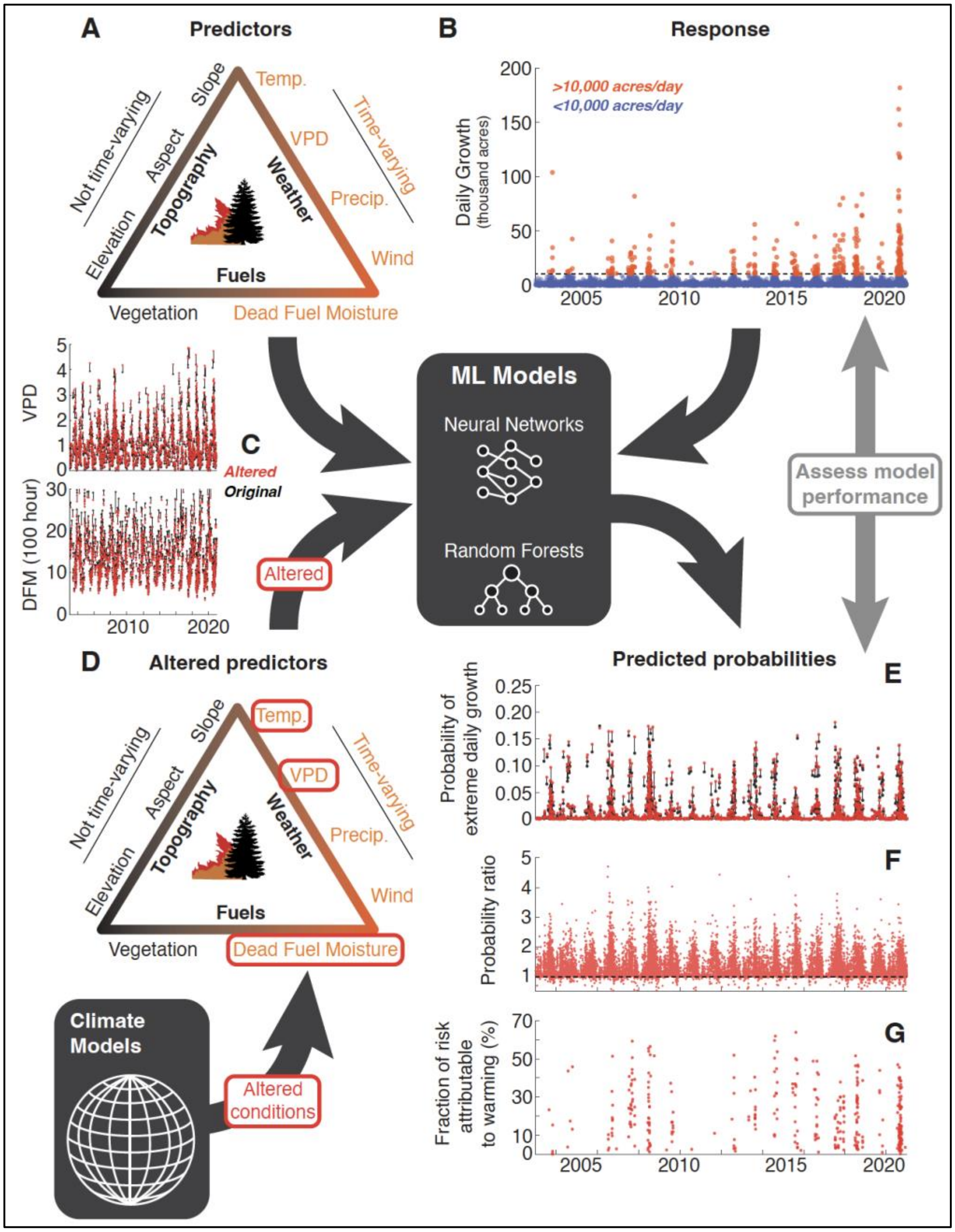

Fig. 1. Illustration of the method. (A, B, C, E) An ensemble of neural networks and random forests learn the relationships between 11 environmental predictor variables (see Table S2) and the probability of occurrence of daily wildfire growth >10,000 acres. (D, C and E) The probability of occurrence calculated is calculated again, incorporating shifts in background climatological temperature produced from Global Climate Models. Temperature changes are also propagated into aridity variables that have a direct relationship with temperature (Eqs. S3-S10). (E) Predicted probability of extreme daily growth for present (red) compared to preindustrial (black) with each event connected by a black line. For clarity, a random sampling of only 2,000 fire-days is displayed. (F) Probability ratios for the two probabilities shown in E (Eq. S1). (F) Fraction of the risk of extreme daily growth attributable to anthropogenic warming (Eq. S2). All results in E, F and G are calculated outside of the training set so that predictive skill can be assessed along with the results. These are calculated using leave-3-years-out cross-validation. All results in E, F and G are averages over the top 10% of machine learning model configurations in terms of their log-loss scores (black dots in Fig. S3A, Fig. S3B, and Fig. S4). See Materials and Methods and a video explanation of the method for further details: https://youtu.be/lHztGWzghRI

Probability ratios for the historical period relative to preindustrial, range from slightly below one to over five but have a mean of 1.33 (Fig. 1F and 2A). For the 380 extreme daily growth events that took place from 2003 to 2020, the fraction of the risk attributable to anthropogenic warming was as high as 65% and had a mean of 19% (Fig. 1G and 2B).

By mid-century, the mean probability ratio continues to increase from 1.33 and ranges from 1.93 in the SSP1-2.6 low emissions scenario (roughly in line with the Paris Agreement) to 2.48 in the SSP5-8.5 very high emissions scenario (Fig. 2C and Fig. 2E). Under the low emissions scenario, the mean probability ratio is essentially stabilized from mid-century onward as it only increases to 1.96 by the end of the century (Fig. 2D). On the other hand, under the very high emissions scenario, the average probability ratio reaches 5.88 by the end of the century (Fig. 2F), indicating that future emissions have large leverage on future extreme wildfire behavior.

The shifts in daily risk indicate that the historical period has experienced an aggregate expected increase in extreme daily growth frequency of 25% relative to preindustrial (362 vs. 289, Fig. 2G). Going forward, the expected frequency of occurrence continues to increase through mid-century, but it can be stabilized at an average of +59% (459 vs. 289) at the end of the century under low emissions, compared to +172% (786 vs. 289) at the end of the century under very high emissions (Fig. 2G). It must be emphasized that these are idealized calculations that hold fire-days constant and isolate the influence of temperature and temperature's direct impact on aridity. They are likely to be conservative because they do not incorporate changes in ignition proclivity, fire season length, fire lifetimes, etc.

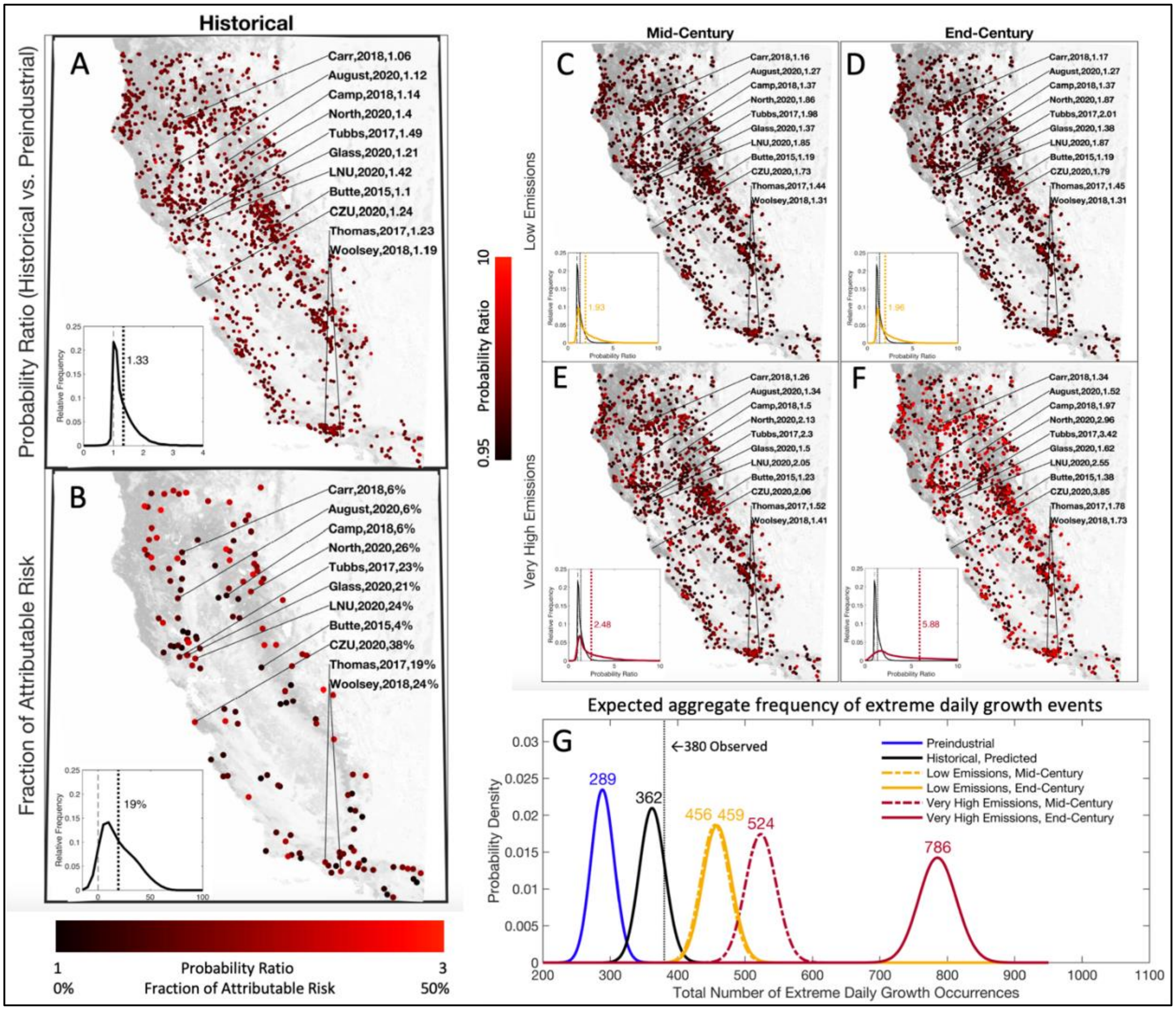

Fig. 2. Anthropogenic warming's influence on the risk of extreme wildfire behavior historically and in the future. (A) Probability ratios for all fire-days in the present relative to preindustrial, averaged over the top 10% of machine learning models (same information as Fig. 1F but displayed in space rather than time). (B) same as (A) but for the fraction of risk attributable to anthropogenic warming and only those fire-days with growth >10,000 acres considered (same information as Fig. 1G but displayed in space rather than time). (C, D, E, F) Probability ratios for all fire-days in the dataset for mid-century (C, E) and end-century (D, F) and for a low emissions scenario (SSP1-2.6, C, D) and a very high emissions scenario (SSP5-8.5, E, F). Fires notable for causing large damage are highlighted. The probability ratios for these fires are calculated as a mean daily probability of extreme growth over the fire's lifetime in the altered climate divided by the mean daily probability over the fire's lifetime in the preindustrial climate (as opposed to the mean of the daily probability ratios, see Eqs. S19 and S20). Insets are kernel density estimates fit to the probability ratio distributions across all fire-days. Vertical lines in the insets are the distribution means. The historical distribution (black) is reproduced in C-F for context. (G) Poisson distributions for the expected aggregate frequency of extreme growth days for historical fire-days under different background climatological temperatures.

Figures 3A and 3B show the effect of propagating temperature into all combinations of the four temperature-responsive predictor variables. The highest probability ratios and fractions of attributable risk are calculated when temperature change is propagated into all three aridity predictors in addition to temperature itself (far left column of Fig. 3A and Fig. 3B). When only propagating into three variables, the three aridity variables have the largest impact. When only propagating into two variables, vapor pressure deficit and 100 hour dead fuel moisture have the largest impact, and when propagating into only one variable, 100 hour dead fuel moisture has the largest impact. In all combinations, the direct effect of temperature is the least important variable, confirming that temperature's impact is felt primarily through its effect on the atmospheric capacity for water vapor and thus fuel moisture (*11, 12, 28*).

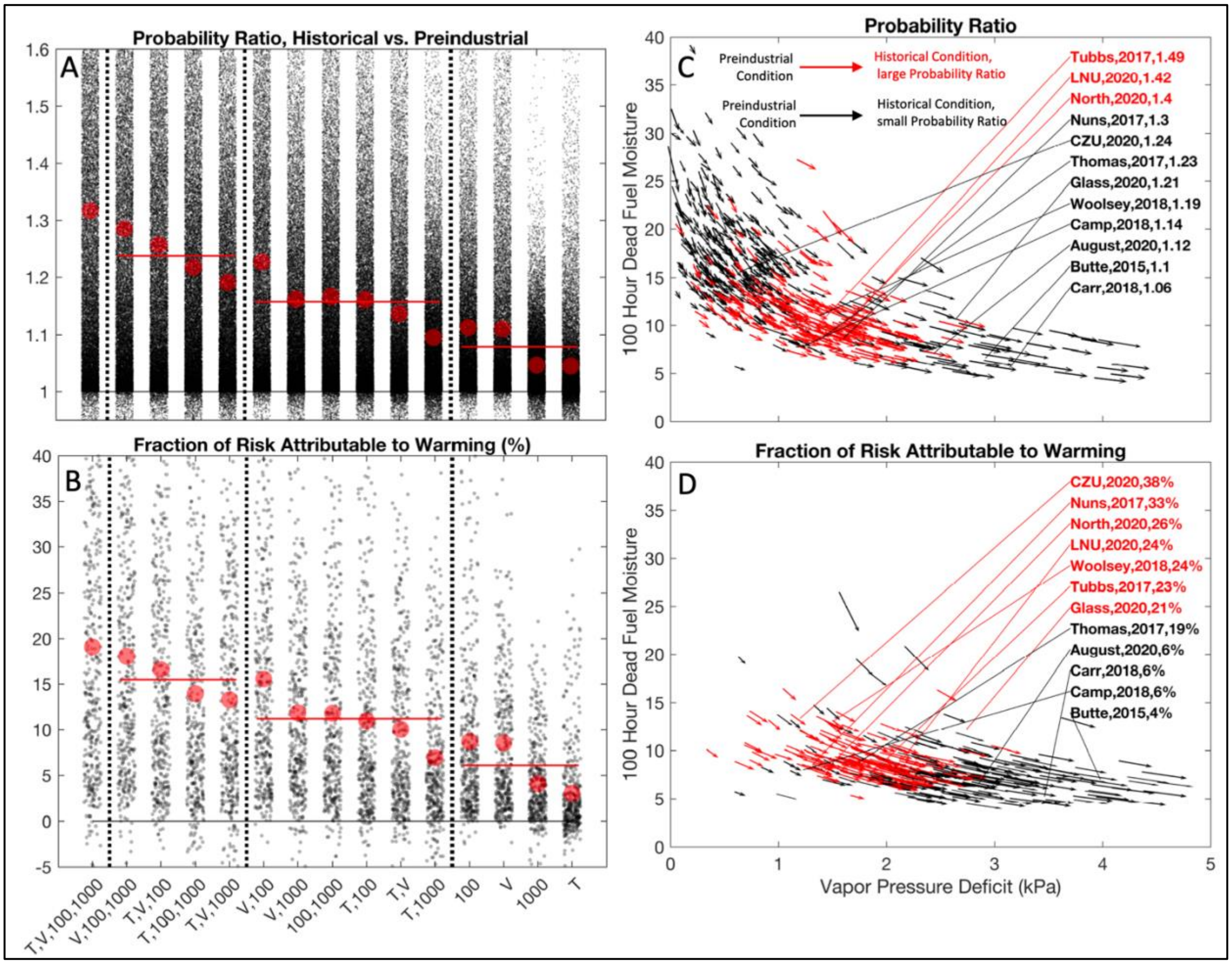

Fig. 3. Physical conditions and mechanisms most responsible for shifts in the risk of extreme wildfire growth. (A and B) the effect of propagating anthropogenic warming into different combinations of the four predictors directly influenced by temperature. Each grey dot represents a fire-day, and the red circles are distribution means (the far left column in A and B show the same distributions as the insets in Fig. 2A and 2B). The letters at the bottom show which predictors changes in temperature are propagated into, where T=temperature, V = vapor pressure deficit, 100 = 100 hour dead fuel moisture, and 1000 = 1,000 hour dead fuel moisture. (C) The shift in 100 hour dead fuel moisture and vapor pressure deficit for 800 randomly selected fire-days from the dataset. (D) same as (C) but for all 380 extreme growth days. In C and D, the origin of each arrow represents that fire-day's conditions in the preindustrial climate, and the tip of each arrow represents the conditions for the historical period. Red indicates that a probability ratio (C) or fraction of attributable risk (D) is above the mean value of the distribution. Above average probability ratios and fractions of attributable risk are centered near about 10% 100 hour dead fuel moisture and about 1.5 kPa vapor pressure deficit, indicating that these values represent important thresholds. Values for fires notable for causing large damage are highlighted where the parameter values are means over the fire's lifetime.

We highlight results for twelve historical fires that were notable for causing a large amount of structural damage (labeled fires in Fig. 2, Fig. 3C, D, and Fig. 4, Fig. S10-S12). We find that anthropogenic warming's influence on the risk of extreme daily growth varies markedly between these fires (Fig. 2). For example, the mean probability ratio over the lifetime of the North Complex Fire was 1.4 at the time of occurrence and would reach 2.96 under very high emissions at the end of the century, while the mean probability ratio over the lifetime of the Carr Fire was only 1.06 at the time of occurrence and would only reach 1.34 under very high emissions at the end of the century. Similarly, for the days that did see extreme growth, the fraction of risk attributable to warming was 26% for the North Complex Fire and only 6% for the Carr Fire. Warmings' influence on risk even varies substantially between days for the same fire (Fig. 4). For example, probability ratios for very high emissions at the end of the century range from below 2 to over 12 for the North Complex Fire over its lifetime (Fig. 4F).

The background climatological change in temperature is relatively uniform (Fig. 1, Fig. S2), so the aforementioned variability in risk change is not primarily due to geographic or seasonal differences in the magnitude of warming. Rather, differences arise because some fire-days are very near critical aridity thresholds that have an outsized impact on the risk of extreme growth. In particular, crossing ~10% 100 hour dead fuel moisture from above and/or crossing ~1.5 kPa vapor pressure deficit from below (the two predictor variables most responsible for relative shifts in probability, Fig. 3A, 3B), greatly enhances the risk of extreme daily growth (Fig. 3C and 3D). Fire-days safely on the moist side or far on the dry side of these thresholds (black arrows in Fig. 2C) do not experience large relative shifts in probability from anthropogenic warming and drying. Also, though it is often noted in this context that saturation vapor pressure increases exponentially with temperature, dead fuel moisture decreases asymptotically with temperature, indicating diminishing returns for warming's impact on fuel moisture (counterclockwise turning of arrows as vapor pressure deficit increases in Fig. 3C and 3D).

The influences of critical thresholds and diminishing returns are seen over the lifetimes of fires as well (Fig. 4). For example, the Carr Fire occurred under very dry conditions such that its daily mean probability of extreme growth was larger under preindustrial conditions than the North Complex Fire's was for very high emissions at the end of the century (cf. Fig. 4C and Fig. 4D). Thus, even under preindustrial conditions, the Carr Fire maintained 100 hour dead fuel moistures below 10% and vapor pressure deficits above 1.5 kPa over its entire life (Fig. 4G and Fig. 4I, respectively), resulting in low probability ratios from anthropogenic warming (Fig. 4E). On the other hand, the North Complex Fire occurred under conditions straddling the critical thresholds (i.e., its growth was weather-limited (*31*)), so anthropogenic warming had a much larger impact on its probability ratios (Fig. 3F). Correspondingly, as day-to-day weather variability moves the entire ensemble of time series away from the thresholds, probability ratios dip to local minimums (e.g., September 3rd – 12th, 2020 for the North Complex Fire (Fig. 4F, 4H, and 4J).

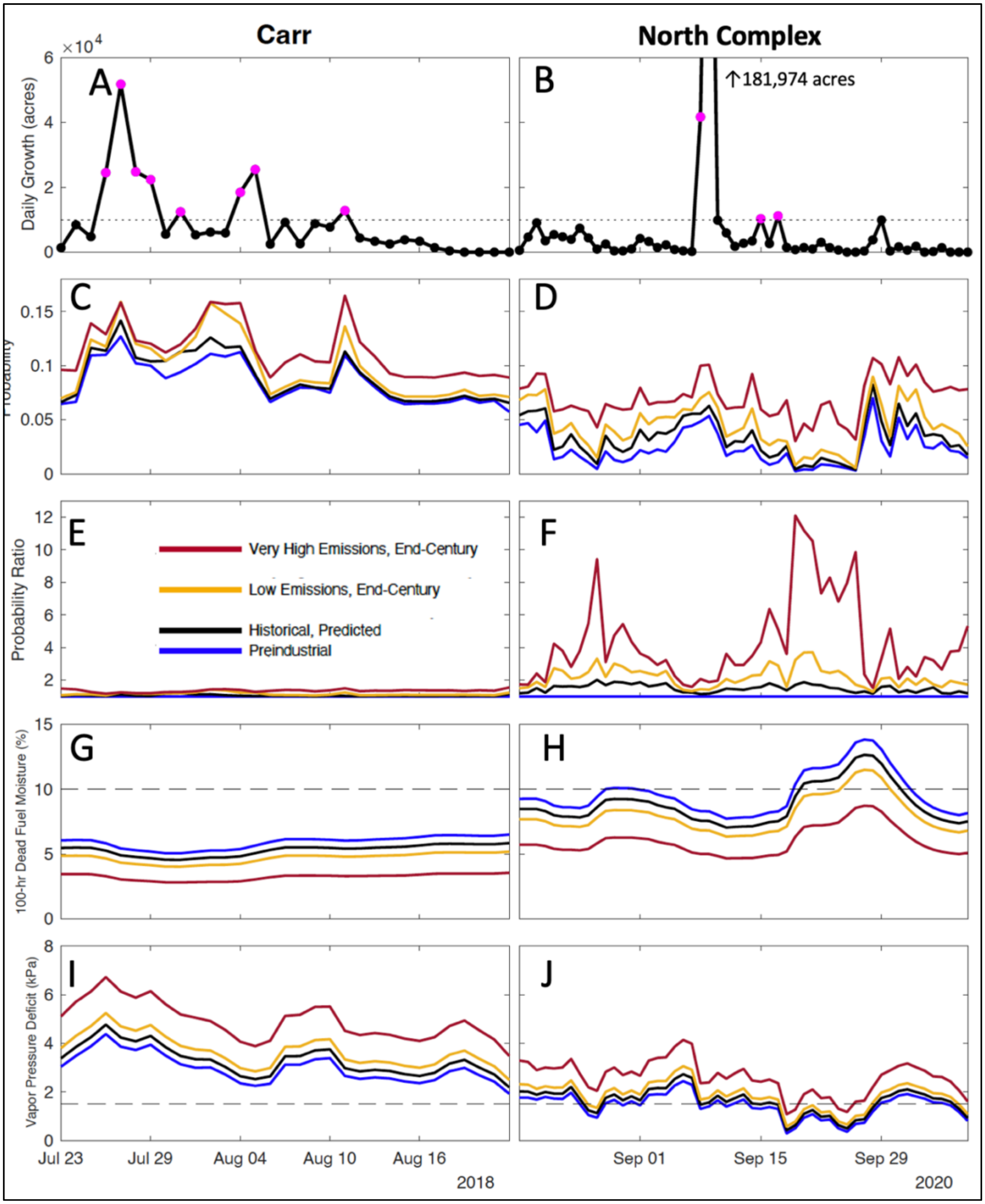

Fig. 4. Anthropogenic warming's influence on the risk of extreme wildfire behavior over the lifetimes of the Carr Fire and the North Complex Fire. (A, B) Daily growth for the fires with extreme daily growth highlighted in magenta. (C, D) Machine learning model calculated risk of extreme daily growth (trained on other fires) under differing levels of anthropogenic warming (legend in panel E). (E, F) Same as (C, D) but change in risk expressed as the probability ratio (Eq. S1) relative to preindustrial risk. (G, H) 100 hour dead fuel moisture percentage. (I, J) Vapor Pressure Deficit (kPa). The preceding two predictor variables are highlighted here because they were found to be the most influential on probability ratios (Fig. 3A and Fig 3B). The same diagrams for the other highlighted fires are shown in Figs S10-S12.

Our results reveal the historical and potential future impact of anthropogenic changes in temperature and aridity (holding all else constant) on extreme daily growth of California wildfire. Since, in reality, climate change involves shifts in vegetation, ignition, and weather patterns, our findings must be interpreted narrowly as idealized calculations that quantify the impact of only a subset of all possible influences of wildfire behavior. Nonetheless, temperature is the most direct response to increasing greenhouse gas concentrations, and there is no theoretical or model consensus on the magnitude or even the sign of the response to many other variables involving changes in atmospheric circulation (*32*). Ultimately, we believe that these calculations result in conservative estimates of changes in risk because many of the variables that we hold constant – vapor pressure (*33*), precipitation (*34*), wind (*10*), tree mortality (*35*), fire season length (*14, 36*), and lifetimes of fires (*2*) – are likely being pushed in a direction that would exacerbate rather than attenuate the risk of extreme wildfire behavior.

References

1. J. D. Coop *et al.*, Extreme fire spread events and area burned under recent and future climate in the western USA. *Global Ecology and Biogeography*, (2022).
2. C. S. Juang *et al.*, Rapid Growth of Large Forest Fires Drives the Exponential Response of Annual Forest-Fire Area to Aridity in the Western United States. *Geophysical Research Letters* **49**, (2022).
3. J. E. Keeley, A. D. Syphard, Large California wildfires: 2020 fires in historical context. *Fire Ecology* **17**, (2021).
4. D. Wang *et al.*, Economic footprint of California wildfires in 2018. *Nature Sustainability*, (2020).
5. D. M. J. S. Bowman *et al.*, Human exposure and sensitivity to globally extreme wildfire events. *Nature Ecology & Evolution* **1**, 0058 (2017).
6. C. F. Starrs, V. Butsic, C. Stephens, W. Stewart, The impact of land ownership, firefighting, and reserve status on fire probability in California. *Environmental Research Letters* **13**, 034025 (2018).
7. D. M. J. S. Bowman *et al.*, Vegetation fires in the Anthropocene. *Nature Reviews Earth & Environment* **1**, 500-515 (2020).
8. J. Mandel *et al.*, Recent advances and applications of WRF–SFIRE. *Natural Hazards and Earth System Sciences* **14**, 2829-2845 (2014).
9. A. Di Luca, A. J. Pitman, D. Elía, Ramón, Decomposing Temperature Extremes Errors in CMIP5 and CMIP6 Models. *Geophysical Research Letters* **47**, (2020).
10. G. Michael *et al.*, Climate change is increasing the risk of extreme autumn wildfire conditions across California. *Environmental Research Letters*, (2020).
11. A. P. Williams *et al.*, Observed Impacts of Anthropogenic Climate Change on Wildfire in California. *Earth's Future* **7**, 892-910 (2019).
12. J. T. Abatzoglou, A. P. Williams, Impact of anthropogenic climate change on wildfire across western US forests. *Proceedings of the National Academy of Sciences* **113**, 11770-11775 (2016).
13. R. Seager *et al.*, Climatology, Variability, and Trends in the U.S. Vapor Pressure Deficit, an Important Fire-Related Meteorological Quantity. *Journal of Applied Meteorology and Climatology* **54**, 1121-1141 (2015).
14. W. M. Jolly *et al.*, Climate-induced variations in global wildfire danger from 1979 to 2013. *Nature Communications* **6**, 7537 (2015).
15. G. J. Van Oldenborgh *et al.*, Attribution of the Australian bushfire risk to anthropogenic climate change. *Natural Hazards and Earth System Sciences* **21**, 941-960 (2021).
16. J. T. Abatzoglou, A. P. Williams, R. Barbero, Global Emergence of Anthropogenic Climate Change in Fire Weather Indices. *Geophysical Research Letters* **46**, 326-336 (2019).
17. P. Jain, D. Castellanos-Acuna, S. C. P. Coogan, J. T. Abatzoglou, M. D. Flannigan, Observed increases in extreme fire weather driven by atmospheric humidity and temperature. *Nature Climate Change* **12**, 63-70 (2022).
18. S. S. C. Wang, Y. Qian, L. R. Leung, Y. Zhang, Identifying Key Drivers of Wildfires in the Contiguous US Using Machine Learning and Game Theory Interpretation. *Earth's Future* **9**, (2021).

19. Y. Huang, Y. Jin, M. W. Schwartz, J. H. Thorne, Intensified burn severity in California's northern coastal mountains by drier climatic condition. *Environmental Research Letters* **15**, 104033 (2020).
20. M. Elia *et al.*, Estimating the probability of wildfire occurrence in Mediterranean landscapes using Artificial Neural Networks. *Environmental Impact Assessment Review* **85**, 106474 (2020).
21. O. Satir, S. Berberoglu, C. Donmez, Mapping regional forest fire probability using artificial neural network model in a Mediterranean forest ecosystem. *Geomatics, Natural Hazards and Risk* **7**, 1645-1658 (2016).
22. P. A. Werth *et al.*, "Synthesis of Knowledge of Extreme Fire Behavior: Volume 2 for Fire Behavior Specialists, Researchers, and Meteorologists," (U.S. Forest Service, General Technical Report PNW-GTR-891, 2016).
23. C. Schär, C. Frei, D. Lüthi, H. C. Davies, Surrogate climate-change scenarios for regional climate models. *Geophysical Research Letters* **23**, 669-672 (1996).
24. C. M. Patricola, M. F. Wehner, Anthropogenic influences on major tropical cyclone events. *Nature* **563**, 339-346 (2018).
25. S. I. Seneviratne *et al.* (Cambridge University Press, Cambridge, United Kingdom and New York, NY, USA, 2021).
26. F. E. L. Otto, Attribution of Weather and Climate Events. *Annual Review of Environment and Resources* **42**, 627-646 (2017).
27. B. E. Potter, D. Mcevoy, Weather Factors Associated with Extremely Large Fires and Fire Growth Days. *Earth Interactions*, 1-53 (2021).
28. A. Gutierrez Aurora *et al.*, Wildfire response to changing daily temperature extremes in California's Sierra Nevada. *Science Advances* **7**, eabe6417.
29. S. Philip *et al.*, A protocol for probabilistic extreme event attribution analyses. *Advances in Statistical Climatology, Meteorology and Oceanography* **6**, 177-203 (2020).
30. N. L. Bindoff, P.A. Stott, K.M. AchutaRao, M.R. Allen, N. Gillett, D. Gutzler, K. Hansingo, G. Hegerl, Y. Hu, S. Jain, I.I. Mokhov, J. Overland, J. Perlwitz, R. Sebbari and X. Zhang, "In: Climate Change 2013: The Physical Science Basis. Contribution of Working Group I to the Fifth Assessment Report of the Intergovernmental Panel on Climate Change," (Cambridge University Press, Cambridge, United Kingdom and New York, NY, USA.).
31. A. Duane, M. Castellnou, L. Brotons, Towards a comprehensive look at global drivers of novel extreme wildfire events. *Climatic Change* **165**, (2021).
32. T. Woollings *et al.*, Blocking and its Response to Climate Change. *Current Climate Change Reports* **4**, 287-300 (2018).
33. Y. Zhuang, R. Fu, B. D. Santer, R. E. Dickinson, A. Hall, Quantifying contributions of natural variability and anthropogenic forcings on increased fire weather risk over the western United States. *Proceedings of the National Academy of Sciences* **118**, e2111875118 (2021).
34. D. L. Swain, A Shorter, Sharper Rainy Season Amplifies California Wildfire Risk. *Geophysical Research Letters* **48**, (2021).
35. S. L. Stephens *et al.*, Drought, Tree Mortality, and Wildfire in Forests Adapted to Frequent Fire. *BioScience* **68**, 77-88 (2018).
36. A. L. Westerling, Increasing western US forest wildfire activity: sensitivity to changes in the timing of spring. *Philosophical Transactions of the Royal Society B: Biological Sciences* **371**, 20150178 (2016).
37. M. A. Moritz, M. E. Morais, L. A. Summerell, J. M. Carlson, J. Doyle, Wildfires, complexity, and highly optimized tolerance. *Proceedings of the National Academy of Sciences of the United States of America* **102**, 17912-17917 (2005).
38. P. Pall *et al.*, Anthropogenic greenhouse gas contribution to flood risk in England and Wales in autumn 2000. *Nature* **470**, 382-385 (2011).
39. D. A. Stone, M. R. Allen, The End-to-End Attribution Problem: From Emissions to Impacts. *Climatic Change* **71**, 303-318 (2005).
40. V. Eyring *et al.*, Overview of the Coupled Model Intercomparison Project Phase 6 (CMIP6) experimental design and organization. *Geoscientific Model Development* **9**, 1937-1958 (2016).
41. K. Riahi *et al.*, RCP 8.5—A scenario of comparatively high greenhouse gas emissions. *Climatic Change* **109**, 33-57 (2011).
42. Z. G. P. P. Hausfather, *Nature* **577**, 618-620 (2020).
43. M. G. Burgess, J. Ritchie, J. Shapland, R. Pielke, IPCC baseline scenarios have over-projected CO2 emissions and economic growth. *Environmental Research Letters* **16**, 014016 (2021).
44. R. Benedetti, Scoring Rules for Forecast Verification. *Monthly Weather Review* **138**, 203-211 (2010).

45. G. W. Brier, VERIFICATION OF FORECASTS EXPRESSED IN TERMS OF PROBABILITY. *Monthly Weather Review* **78**, 1-3 (1950).
46. R. C. Rothermel. (U.S. Department of Agriculture, Forest Service, Intermountain Research Station, 1991).
47. N. P. Lareau, C. B. Clements, Environmental controls on pyrocumulus and pyrocumulonimbus initiation and development. *Atmospheric Chemistry and Physics* **16**, 4005-4022 (2016).
48. J. Mandel, J. D. Beezley, A. K. Kochanski, Coupled atmosphere-wildland fire modeling with WRF 3.3 and SFIRE 2011. *Geoscientific Model Development* **4**, 591-610 (2011).

Acknowledgments:

We acknowledge the PG&E meteorology operations and fire science team for guidance and discussion throughout the project. We acknowledge teams at DTN (https://www.dtn.com/), Atmospheric Data Solutions (http://www.atmosphericdatasolutions.com/), and Sonoma Technology (http://www.sonomatech.com/) for data preprocessing and preparation. We also acknowledge Mike Voss for technical support and A.J. Eiserloh, Richard Bagley, and Pardeep Pall for valuable discussions.

Funding:

This project was funded from a contract (#C6909) between PG&E and San José State University Research Foundation titled "Understanding Extreme Fire Weather Conditions using a 30-year High-Resolution WRF Model Dataset".

Competing interests:

We have no financial conflicts of interest to report.

Two common interests that are not always aligned with objective truth-seeking in research are 1) The career incentive to publish interesting results in high profile journals and 2) The sociopolitical culture surrounding researchers, which influences what results are thought to be desirable. These forces inevitably affect the questions researchers ask and the level of scrutiny that researchers apply to initial findings. We do not claim that we are immune to these influences, but we are at least cognizant of them and have tried to mitigate them as much as possible by explicitly contemplating how the research might be done under different circumstances with different incentives.

Data and materials availability: The code for this study is archived at https://github.com/ptbrown31/Climate-Driven-Risk-of-Extreme-Wildfire-in-California. The WRF model is open source and can be downloaded at https://github.com/wrf-model/WRF/releases. MODIS fire products can be downloaded at https://firms.modaps.eosdis.nasa.gov/active_fire/, and the CMIP6 climate model data can be downloaded at https://interactive-atlas.ipcc.ch/regional-information.

Supplementary Material / Materials and Methods

Overview and concept

The goal of the study is to assess anthropogenic warming's influence on the risk of extreme wildfire behavior in California using an empirical approach where the relationship between temperature and the risk of extreme wildfire behavior is learned from 17,910 geographically dispersed fire-days in California from 2003-2020. We also seek to make attribution statements at the level of individual fires. See a video explanation of the method here: https://youtu.be/lHztGWzghRI

The extreme wildfire behavior that we focus on is extreme daily growth, specifically 10,000 acres or more in a day. This threshold was chosen because it's extreme enough to embody the outsized impact we are interested in, but it is not too extreme such that there are only a handful of events to study. Since we are specifically interested in the occurrence of these extreme events taking place or not, we convert our wildfire growth data into a binary response variable which indicates if growth above 10,000 acres occurred.

We also characterize the occurrence of the events probabilistically as we treat their occurrence as containing fundamental uncertainty due to incomplete information as well as atmospheric chaos.

We are specifically interested in how a fire's environment (including ambient temperature) influences the risk of extreme daily growth. We therefore use regression models to understand the relationship between the risk of extreme daily growth and a number of predictor variables established to be important influences on wildfire behavior (Fig. 1, Table S2). These predictor variables represent fundamental components of the well-known daily-timescale wildfire behavior triangle (*37*) which has edges of topography, fuels, and weather. We did not prescreen predictors for their predictive skill because we were not trying to optimize for predictive skill over physical understanding. Rather, the predictors were selected so that the models would be able to make predictions about the influence of temperature changes on extreme daily wildfire growth risk conditional on a set of fundamental attributes, like slope and vegetation type.

Many traditional regression methods assume that the influence of any predictor variable is independent of the influence of the other predictor variables and that their influences are monotonic, if not linear. However, it is well known that the influence of any one of our predictor variables will be highly conditional on the state of other predictor variables. Thus, rather than use traditional regression methods, we build on recent work in the field (*18-21*) and implement machine learning models (specifically neural networks and random forests) in order to estimate the associations between the environmental conditions (or predictors) and the risk of extreme daily wildfire growth. These models are able to account for non-linear, non-monotonic, and interactive relationships between the predictors without the researcher having to presuppose the functional forms of such relationships.

We confirm that these predictors do constrain the risk of extreme wildfire growth using leave-3-years-out cross-validation where each 3-year chunk (2003-2005, 2006-2008,…,2018-2020) is held out in sequence, and the remaining data is used to train the machine learning models. Then the machine learning models make probabilistic predictions of extreme growth on the held-out data, and their performance on that data is assessed using four different scoring metrics (log-loss, Brier, reliability diagram, and the area under the Receiver Operating Characteristic curve, ROC-AUC, Fig. S3A, and Fig. S3B).

We test 1,000 neural network configurations and 1,000 random forest configurations by randomly varying hyperparameters for each (individual dots in Fig. S3A and S3B). The scoring metrics are standardized against a naïve model that always predicts the baseline probability of extreme growth (anything over 1 in the columns labeled "skill score" Fig. S3A and S3B indicated better performance than the naïve model). Our main reported results throughout the manuscript are results that are averaged over the model configurations that performed in the top 10% in the leave-3-years-out cross-validation test. These top 10% models are indicated with small black dots in Fig. S3A and S3B. We also test the models' ability to make predictions outside of their parameter space in the Train on Cool, Test on Warm Experiment discussed below.

The learned relationships take advantage of the large amount of data (which allows for a large exploration of the parameter space) and the large variance in the feature variables that are dominated by geographic, seasonal, and weather variability as opposed to long-term trends. This means that factors like the long-term increase in fuel buildup or the long-term expansion of human population into the wildland-urban interface do not co-vary with temperature in this dataset and thus are not confounding factors in the way they are on, e.g., long-term annual area-burned trends.

Because the learned relationships are associational, they cannot strictly be considered causal, though knowledge of the physical world, for example, that fuels burn more readily when they are drier, can be used to supplement the associations found in the data to make reasonably confident inferences about causality.

Broadly speaking, our approach can be summarized in two steps:

1) Learn relationships between environmental conditions and the risks of extreme daily fire growth for historical fires from 2003 to 2020

2) Recalculate the risks under altered background climatological temperatures associated with anthropogenic warming

We compare the probabilities of extreme daily growth calculated with the original predictor values to those calculated with the altered predictor values using a probability ratio (*29*),

$$Probability\ Ratio = \frac{P(extreme\ daily\ growth\mid warmed\ temperatures)}{P(extreme\ daily\ growth\mid preindustria\ temperatures)}. \qquad S1$$

A Probability ratio of 1.5, for example, would mean that the climatological temperature change being considered made the risk of extreme daily growth 50% more likely.

Also, for historical fire-days that did see extreme daily growth, we can calculate the fraction of the risk of that event occurring that was due to climatological temperature change – the Fraction of Attributable Risk (*30*, *38*, *39*)

$$Fraction\ of\ Attributable\ Risk\ = 1 - \frac{1}{Probability\ Ratio\ for\ an\ extreme\ growth\ day}. \qquad S2$$

The altered background climatological temperatures come from multi-decadal and multi-model means produced by global climate models (Table S1, (*40*)). These climatological changes in temperature are a function of space and the month of the year.

It is already well-established that anthropogenic warming's influence on wildfire behavior is not primarily via temperature per se but rather through temperature's influence on aridity. Thus, when attempting to assess anthropogenic warming's influence on the risk of extreme wildfire behavior, we must also consider temperature's influence on aridity predictors that have a direct relationship with temperature. Accordingly, we also propagate changes in temperature into the daily mean vapor pressure deficit (which influences the aridity of fine fuels), 100 hour dead fuel moisture, and 1,000 hour dead fuel moisture (which represent fuel moistures for fuels of different sizes and thus different response times). Both of these dead fuel moisture variables experience the background climatological change in temperature over a period of 125 days prior to the fire day (Eqs S5-S10).

We test the influence (on risk change) of propagating temperature into every possible predictor combination and find that 100 hour dead fuel moisture has the largest influence while temperature itself has the smallest influence (Fig. 3A and 3B).

Every other predictor variable other than temperature and the three aridity metrics is held constant in our procedure, including topography, vegetation characteristics, precipitation, wind, and absolute moisture content of the atmosphere (vapor pressure). Conceptually, the question being asked is:

> "What if everything in terms of weather and ignitions over 2003-2020 was the same, except the background temperature was changed to be like the 1850-1900 average, or the 2041-2060 average, or the 2081-2100 average under different emissions scenarios?"

We believe this experiment design results in conservative estimates of the change in risk as there is evidence that many of the predictors that are held constant are likely being pushed in a direction that would exacerbate rather than attenuate the risk of extreme wildfire growth.

Our approach is similar to the established "Pseudo-Global Warming" or "Storyline" approaches in the extreme event attribution literature (*24*, *25*), which also hold almost everything about a given weather event constant except for a small handful of variables of interest.

The difference, however, is that in the "Pseudo-Global Warming" or "Storyline" approaches, the influence of the independent variable (temperature, for example) on the extreme weather event is typically quantified through a physical or mechanistic model that calculates interactions through a conglomeration of physical equations and semi-empirical parameterizations. Our approach is similar in principle, but the models that quantify the influence of the independent variable on the extreme event are machine learning models that have learned the empirical relationships directly from the data. To reiterate, the advantage of using machine learning models is that the relationships can be quantified more accurately than in some mechanistic models, but the disadvantage is that relationships are associational by definition and cannot be interpreted as causal.

An advantage of holding everything about the weather during fire-days constant and thus isolating the influence of temperature alone (as well as temperatures influence on aridity) is that our confidence in long-time-mean temperature changes simulated by global climate models is higher than our confidence in any other predictor variable output from global climate models and higher than our confidence in simulated changes in the aggregate statistics of daily weather extremes.

Using anthropogenic warming calculated from global climate models, the trained machine learning models can then make altered predictions of the probability of extreme daily growth on the same historical fire-days but under different background climatological temperatures.

In our procedure, the out-of-training-sample predictions and shifts in future probability are calculated by the same model fit on the same training data in the cross-validation procedure, so the models never have access to predictor information for any fire-day that they are assigning a probability to, either using original or altered predictor values.

Due to the output of our method being fundamentally probabilistic, it also has similarities to the "Probability-based approach" of the extreme event attribution literature (*25*). Thus, with its conceptual similarity to the "Probability-based approach" as well as the "storyline approach", we refer to our method as the "Probabilistic-Storyline Approach" for extreme event attribution.

Further details on the predictors, response, machine learning models, methods, and sensitivity tests are provided below. See also a video explanation of method: https://youtu.be/lHztGWzghRI

Response Data (daily fire growth)

Geolocated daily fire growth from 2003 to 2020 within California state lines was calculated from raw fire detect data obtained from the MODIS system on NASA's Terra and Aqua satellites by a team at Sonoma Technology (http://www.sonomatech.com/). Analysis was restricted to the state of California because the dataset was created for use by the Pacific Gas and Electric Company (PG&E) whose territory is contained within California.

We only investigate fire-days that occurred in nine land categories defined in the Weather Research and Forecasting (WRF) model. We aggregated these nine categories to three categories in our predictor dataset representing either Forest (Category 1), Shrub (Category 2), or Savanna/Grassland (Category 3). We also restricted the analysis to locations with at least 20% vegetation fraction. After this initial filtering, there are 17,910 fire-days in our dataset and 380 instances of extreme daily growth (10,000 acres in a day), which we treat as an "event". The set-up of the binary classification problem is shown in Table S2.

Predictor Data

The 11 predictor variables (Table S2) used as input to the machine learning models were obtained from a high resolution (2km×2km, hourly) reanalysis produced from the National Center for Atmospheric Research's (NCAR) Weather Research and Forecasting (WRF) model (version 4.1.2). The WRF model is open source and can be downloaded at https://github.com/wrf-model/WRF/releases. The National Centers for Environmental Prediction's (NCEP) Climate Forecast System Version Reanalysis (*30*) provided initial and boundary conditions (every 6 hours) for the high-resolution WRF reanalysis. CFSR was used prior to 2011, and CFSv2 was used after 2011.

The WRF reanalysis was produced to complement PG&E's Operational Mesoscale Modelling System (POMMS). The WRF model was tested and validated by teams at DTN (https://www.dtn.com/) and Atmospheric Data Solutions (http://www.atmosphericdatasolutions.com/). Roughly 20 model configurations were tested against a network of hundreds of weather stations in California (from ASOS, PG&E, and RAWS), and the configuration below was deemed to be optimal for PG&E's needs in operational forecasting with a particular emphasis on fire-weather forecasting.

Nested grid resolutions: 18, 6, 2km; Model top pressure level: 20mb; Land use: MODIS30s with lakes (modis_landuse_20class_30s_with_lakes); Land Surface Model: NoahMP; Radiation Schemes: RRTMG; Microphysics scheme: Thompson; Planetary Boundary layer scheme: MYNN2.5; Surface layer scheme: MYNN; Cumulus scheme for outer domain: Kain-Fritsch; Topo shading for innermost domain; Slope-dependent radiation for innermost domain; No nudging.

The WRF reanalysis data was originally at the hourly temporal resolution, but all variables were averaged to the daily temporal resolution to match the temporal resolution of the fire growth data. Values of predictors were obtained for each fire-day in the dataset by using the value of the grid box closest to the latitude and longitude of fire ignition. The 2km resolution portion of the domain excluded the southeastern portion of California (innermost box in Fig. S1).

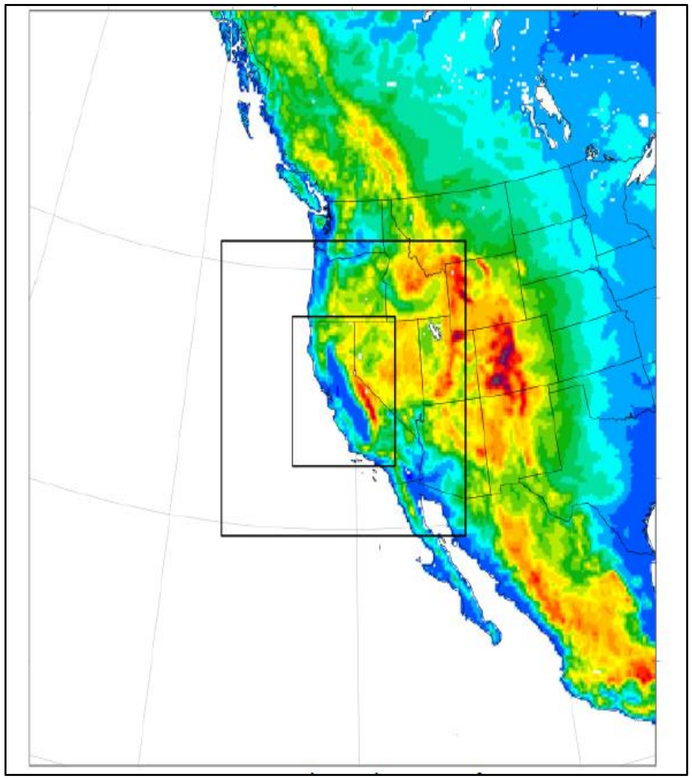

Fig. S1. WRF reanalysis domain configuration (used for predictor values) with elevation shaded. The outer-most domain has a grid spacing of 18km, the middle domain has a grid spacing of 6km, and the inner-most domain (the domain of this study) has a grid spacing of 2km. Data and figure were produced from a partnership between DTN, ADS, and PG&E.

Calculations of Background Anthropogenic Temperature Change.

Background anthropogenic warming was obtained from 34 Global Climate Models (GCMs) that participated in the Coupled Model Intercomparison Project – Phase 6 (CMIP6, Table S1). The following procedure was implemented.

1) The mean temperature was calculated across three time periods: 1850-1900 in the historical experiment, 2041-2060, and 2081-2100 in the SSP1-2.6, SSP2-4.5, and SSP5-8.5 emissions scenarios. This was obtained from the IPCC WGI Interactive Atlas (https://interactive-atlas.ipcc.ch/regional-information). Data were downloaded separately for each month of the year and as a function of space on a $1^{o}\times1^{o}$ grid over our domain.

2) Data was bilinearly interpolated to our fire-day locations.

3) A mean temperature was calculated for the current period 2003-2020 by interpolating in time between the 1995-2014 value and the 2041-2060 value (for each month of the year and grid point over our domain). Given that the two endpoints were 20-year means, the interpolated value was also a 20-year mean but centered on the 2003-2020 period.

4) Temperature changes were calculated all relative to the 2003-2020 period, so no climatological mean biases would be allowed to affect the analysis (Fig. S2).

5) Temperature changes were incorporated into predictors for all the fire-days.

We note that the SSP5-8.5 emissions scenario is thought to be a very high and thus unlikely scenario (*41*). It is inconsistent with current projections of energy systems over the remainder of the century (*42*, *43*). Nevertheless, even if SSP5-8.5 emissions levels are now outside of projections associated with economic growth and energy systems, greenhouse gas concentrations could approach those associated with the SSP5-8.5 scenario if carbon cycle feedbacks are on the positive end of their uncertainty range. Furthermore, including SSP5-8.5 in our analysis allows us to calculate probability ratios associated with temperature changes that are very much still on the table, even if they were to occur sometime in the 22^{nd} or 23^{rd} centuries rather than in the period described here (2081-2100).

Table S1. CMIP6 Models used in this study. Model availability and use in this study are denoted with an X.

					Projections 2041-206 and 2081-2100			Res		ESGF versions	Ensemble
	Model	Historical (1850-1900)	Historical (1995-2014)	Interpolated 2001-2020	SSP1-2.6	SSP3-4.5	SSP5-8.5	lat	lon		
1	ACCESS-CM2:	X	X	X	X	X	X	1.88º,	1.25º	v20191108	https://doi.org/10.22033/ESGF/CMIP6.4332
2	ACCESS-ESM1-5:	X	X	X	X	X	X	1.88º,	1.25º	v20191115	https://doi.org/10.22033/ESGF/CMIP6.4333
3	AWI-CM-1-1-MR:	X	X	X	X	X	X	0.94º,	0.93º	v20190529	https://doi.org/10.22033/ESGF/CMIP6.2817
4	BCC-CSM2-MR:	X	X	X	X	X	X	1.12º,	1.11º	v20190318	https://doi.org/10.22033/ESGF/CMIP6.3050
5	CAMS-CSM1-0:	X	X	X	X	X	X	1º,	1º	v20191106	https://doi.org/10.22033/ESGF/CMIP6.11052
6	CANESM5:	X	X	X	X	X	X	2.81º,	2.77º	v20190429	https://doi.org/10.22033/ESGF/CMIP6.3696
7	CESM2:	X	X	X	X	X	X	1.25º,	0.9º	v20200528	https://doi.org/10.22033/ESGF/CMIP6.7768
8	CESM2-WACCM:	X	X	X	X	X	X	1.25º,	0.94º	v20200702	https://doi.org/10.22033/ESGF/CMIP6.10115
9	CMCC-CM2-SR5:	X	X	X	X	X	X	1º,	1º	v20200622	http://doi.org/10.22033/ESGF/CMIP6.3896
10	CNRM-CM6-1:	X	X	X	X	X	X	1.41º,	1.39º	v20190219	https://doi.org/10.22033/ESGF/CMIP6.4224
11	CNRM-CM6-1-HR:	X	X	X	X	X	X	0.5º,	0.5º	v20191202	https://doi.org/10.22033/ESGF/CMIP6.4225
12	CNRM-ESM2-1:	X	X	X	X	X	X	1.41º,	1.39º	v20191021	https://doi.org/10.22033/ESGF/CMIP6.4226
13	EC-EARTH3:	X	X	X	X	X	X	0.7º,	0.7º	v20200310	https://doi.org/10.22033/ESGF/CMIP6.4912
14	EC-EARTH3-Veg:	X	X	X	X	X	X	0.7º,	0.7º	v20200225	https://doi.org/10.22033/ESGF/CMIP6.4914
15	FGOALS-g3:	X	X	X	X	X	X	2º,	5.18º	v20190819	https://doi.org/10.22033/ESGF/CMIP6.3503
16	GFDL-CM4:	X	X	O	O	X	X	1.25º,	1º	v20180701	https://doi.org/10.22033/ESGF/CMIP6.9268
17	GFDL-ESM4:	X	X	X	X	X	X	1.25º,	1º	v20180701	https://doi.org/10.22033/ESGF/CMIP6.8706
18	HADGEM3-GC31-LL:	X	X	X	X	X	X	1.88º,	1.25º	v20200114	https://doi.org/10.22033/ESGF/CMIP6.10901
19	IITM-ESM:	X	X	X	X	X	X	2º,	2º	v20200915	https://doi.org/10.22033/ESGF/CMIP6.44
20	INM-CM4-8:	X	X	X	X	X	X	2º,	1.5º	v20190603	https://doi.org/10.22033/ESGF/CMIP6.12337
21	INM-CM5-0:	X	X	X	X	X	X	2º,	1.5º	v20190724	https://doi.org/10.22033/ESGF/CMIP6.12338
22	IPSL-CM6A-LR:	X	X	X	X	X	X	2.5º,	1.27º	v20190903	https://doi.org/10.22033/ESGF/CMIP6.5271
23	KACE-1-0-G:	X	X	X	X	X	X	1.88º,	1.25º	v20200317	https://doi.org/10.22033/ESGF/CMIP6.8456
24	KIOST-ESM:	X	X	O	O	O	O	1º,	1º		
25	MIROC-ES2L:	X	X	X	X	X	X	2.81º,	2.77º	v20200318	https://doi.org/10.22033/ESGF/CMIP6.5770

26	MIROC6:	X	X	X	X	X	X	1.41º,	1.39º	v20191016	https://doi.org/10.22033/ESGF/CMIP6.5771
27	MPI-ESM1-2-HR:	X	X	X	X	X	X	0.93º,	0.93º	v20190710	https://doi.org/10.22033/ESGF/CMIP6.4403
28	MPI-ESM1-2-LR:	X	X	X	X	X	X	1.88º,	1.85º	v20190710	https://doi.org/10.22033/ESGF/CMIP6.6705
29	MRI-ESM2-0:	X	X	X	X	X	X	1.12º,	1.11º	v20190608	https://doi.org/10.22033/ESGF/CMIP6.6929
30	NESM3:	X	X	X	X	X	X	1.88º,	1.85º	v20190811	https://doi.org/10.22033/ESGF/CMIP6.8790
31	NorESM2-LM:	X	X	X	X	X	X	2.5º,	1.89º	v20191111	https://doi.org/10.22033/ESGF/CMIP6.8319
32	NorESM2-MM:	X	X	X	X	X	X	1.25º,	0.94º	v20191115	https://doi.org/10.22033/ESGF/CMIP6.8321
33	TaiESM1:	X	X	O	O	X	X	1.25º,	0.9º	v20200902	https://doi.org/10.22033/ESGF/CMIP6.9823
34	UKESM1-0-LL:	X	X	X	X	X	X	1.88º,	1.25º	v20190726	https://doi.org/10.22033/ESGF/CMIP6.6405

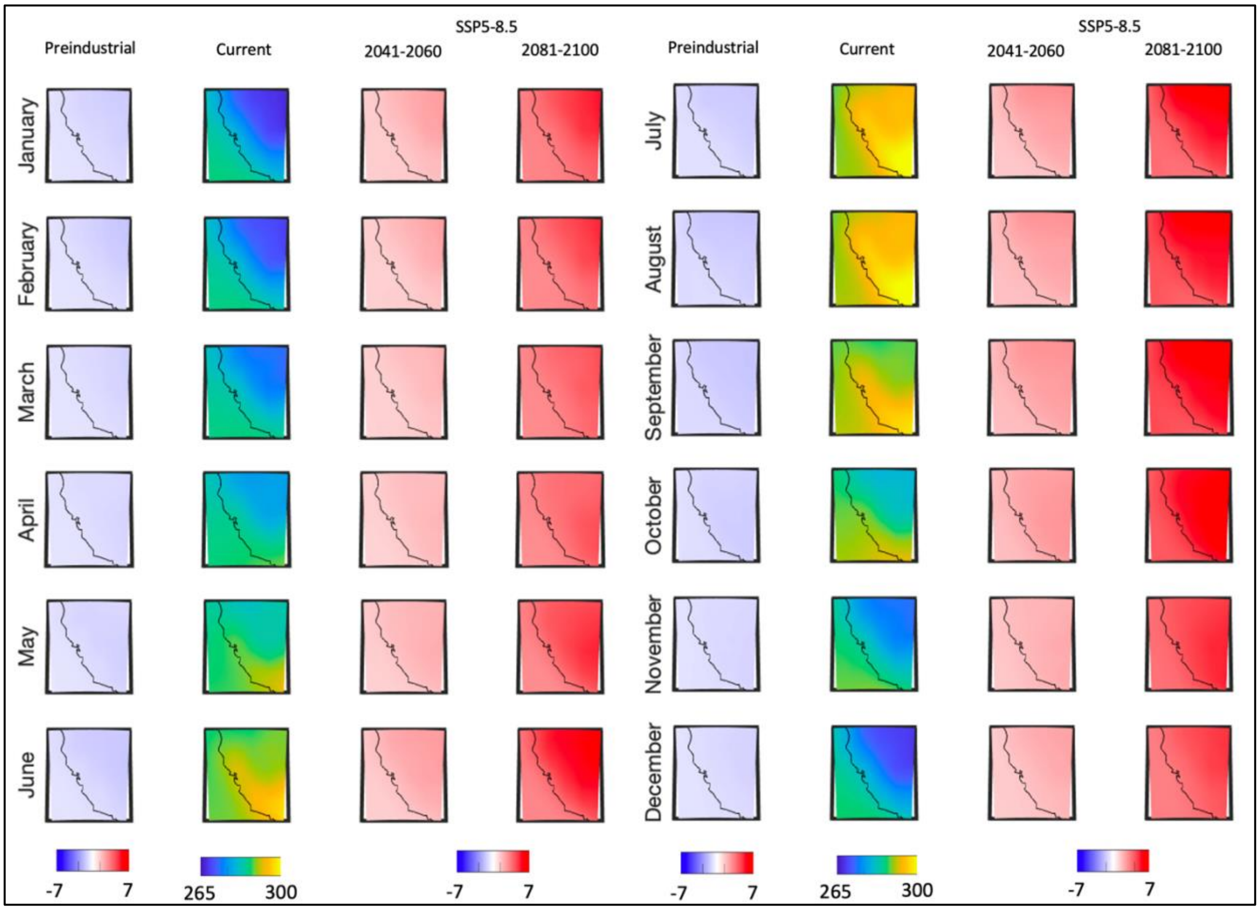

Fig. S2. Structure of background climatological temperature changes imposed on the historical fires from 2003 to 2020. This figure uses SSP5-8.5 as an example. These temperature changes are calculated from the CMIP6 multi-model mean (Table S1) over decade+ time periods in order to 'average out' unforced variability. Their structure is latitude by longitude by month-of-year.

Propagation of Background Temperature Change into Temperature-Dependent Predictors.

GCM-calculated changes in climatological temperature were propagated into the three aridity-related predictors that have a direct relationship with temperature (i.e., it is possible to related them to temperature with a well-known equation or small set of equations, Eqs. S3-S10, Fig. 1C, 1D). These variables are Vapor Pressure Deficit (VPD) and the two dead-fuel moisture variables (100 hour and 1,000 hour). Although temperature inevitably affects precipitation and wind speed, these relationships are less local, less direct, and less certain, so we hold those two variables constant.

Changes in temperature are propagated into the VPD predictor via Saturation Vapor Pressure (SVP),

$$VPD(T) = SVP(T) - VP, \tag{S3}$$

which is exponentially related to temperature. We use a common approximation of this relationship:

$$SVP(T) = 611 \cdot e^{\frac{17.27 \cdot T}{237.3+T}}. \tag{S4}$$

Vapor pressure deficit on the day of the fire is associated with fine fuel moisture. We also propagate temperature directly into two fuel moisture estimates associated with courser fuels: 100 hour and 1,000 hour dead fuel moisture estimates. This is done at all locations regardless of the actual fuel characteristics there (the models must use the other features like land use category and vegetation fraction in combination with calculated dead fuel moisture to learn the circumstances under which dead fuel moisture characteristics are important). The 100 hour and 1,000 hour time-lags (t_L) represent the time it takes a fuel particle to progress 63% of the difference between the current moisture content (m, in kg of water per kg of wood) and the moisture content it would have if it were perpetually under the same environmental conditions, referred to as the equilibrium moisture content (E). 100 hour fuels correspond roughly with particles of 4cm diameter, and 1,000 hour fuels correspond roughly to particles of 7.62cm diameter.

We create estimates of 100 hour and 1,000 hour dead fuel moisture for each fire-day in the dataset via the estimation made in (*8*) by integrating the differential equation

$$\frac{dm}{dt} = \frac{E-m}{t_L} \tag{S5}$$

over 3,000 hours (125 days) prior to the fire-day. Three thousand hours was chosen since it represents the period over which an 1,000 hour particle would reach ~95% of its equilibrium value. The equilibrium value is modified slightly depending on if the moisture content starts above or below the equilibrium value,

$$\frac{dm}{dt} = \begin{cases} \frac{E_d - m}{t_L} \; if \; m > E_d \\ 0 \; if \; E_d \geq m \geq E_w, \\ \frac{E_w - m}{t_L} \; if \; m < E_w \end{cases} \tag{S6}$$

where E_d is the drying equilibrium and E_w is the wetting equilibrium,

$$E_d(T) = 0.924 \cdot RH(T)^{0.679} + 0.000499 \cdot e^{0.1 \cdot RH(T)} + 0.18 \cdot (21.1 + 273.15 - T)\left(1 - e^{-0.115 \cdot RH(T)}\right) \tag{S7}$$

$$E_w(T) = 0.618 \cdot RH(T)^{0.753} + 0.000454 \cdot e^{0.1 \cdot RH(T)} + 0.18 \cdot (21.1 + 273.15 - T)\left(1 - e^{-0.115 \cdot RH(T)}\right) \qquad \text{S8}$$

Also, when it rains (r, mm/h), the equilibrium moisture is replaced by the saturation moisture contents S, and the fuel moisture equation is modified to achieve the rain-wetting lag time t_r,

$$\frac{dm}{dt} = \frac{S-m}{t_r}\left(1 - e^{-\frac{r-r_0}{r_s}}\right), if\ r > r_0. \qquad \text{S9}$$

We propagate changes in temperature into the 100 hour and 1,000 hour dead fuel moisture features by adjusting temperature directly in the equations above as well as adjusting relative humidity in accordance with SVP's response to the temperature change,

$$RH(T) = \frac{VP}{SVP(T)}. \qquad \text{S10}$$

See (*8*) for further discussion. Overall the 100 hour and 1,000 hour dead fuel moisture predictors provide information on the aridity experienced by a location over the antecedent weeks and months, and our results indicate that this information is more important for predicting extreme daily growth than temperature itself.

Table S2. Example of data fed into the modeling framework

Fire Information not used by the models						**Response**		**Predictors**										
Fire_ID	Date	Ignition lat	Ignition lon		daily fire growth acres	Growth above 10,000 acres?		daily mean temperature	daily mean VPD	precip mean past 125 days	Daily mean wind speed	daily mean dead fuel moisture 100 hr	daily mean dead fuel moisture 1000 hr	slope	aspect	elevation	land use category	vegetation fraction
2003_1	1/2/03 0:00	35.30	-118.41		193.99	0		282.80	0.81	0.07	5.80	21.03	15.54	2.44	'4'	970.2042	'2'	27.77
2003_5	1/6/03 0:00	33.94	-117.62		4274.56	0		291.17	1.62	0.03	9.11	12.17	14.19	0.37	'3'	170.9051	'3'	33.16
2003_7	1/7/03 0:00	34.05	-118.87		1990.06	0		293.39	1.78	0.04	8.92	10.94	15.81	4.88	'3'	209.7267	'2'	33.83
2003_8	1/8/03 0:00	41.36	-123.85		193.99	0		288.70	1.31	0.28	2.40	49.53	26.55	10.06	'3'	489.9456	'1'	90.48
2003_9	1/8/03 0:00	40.60	-122.50		387.97	0		284.58	0.70	0.30	2.08	41.78	24.45	1.17	'1'	400.6298	'1'	75.01
2003_10	1/8/03 0:00	39.47	-123.68		193.99	0		289.88	1.28	0.22	2.33	46.04	27.61	1.27	'3'	176.5472	'1'	89.86
2003_13	1/13/03 0:00	34.42	-118.79		785.53	0		288.22	0.85	0.05	3.78	15.63	13.64	2.00	'2'	212.4662	'2'	29.76
2003_14	1/13/03 0:00	34.38	-118.86		193.99	0		287.73	0.81	0.05	3.87	16.54	14.17	4.14	'4'	291.4915	'2'	29.36
2003_15	1/13/03 0:00	34.33	-119.17		383.43	0		287.17	0.61	0.07	1.53	17.61	15.99	2.77	'2'	235.0125	'2'	27.08
2003_18	1/17/03 0:00	38.54	-122.48		193.99	0		286.70	0.86	0.18	2.16	28.58	22.25	3.34	'3'	160.9028	'1'	61.65
2003_19	1/17/03 0:00	41.36	-120.84		193.99	0		279.64	0.62	0.11	2.78	23.38	19.00	4.12	'1'	1671.546	'1'	64.89
2003_20	1/18/03 0:00	38.34	-120.57		193.99	0		286.42	1.01	0.14	2.44	15.95	17.44	1.08	'3'	832.7508	'1'	59.80
2003_21	1/19/03 0:00	40.37	-122.42		788.28	0		283.97	0.23	0.13	0.96	26.43	19.14	0.44	'1'	167.6649	'3'	36.93
2003_22	1/20/03 0:00	38.52	-120.86		575.91	0		283.43	0.36	0.11	2.12	18.86	17.37	1.92	'4'	358.6583	'3'	45.65
2003_23	1/20/03 0:00	39.38	-121.27		976.78	0		284.84	0.64	0.20	1.62	20.44	19.72	1.56	'2'	493.6429	'3'	44.84
2003_24	1/21/03 0:00	40.71	-123.87		193.99	0		284.12	0.32	0.33	5.42	23.75	26.79	5.00	'1'	482.8854	'1'	92.37
2003_25	1/21/03 0:00	36.50	-120.91		383.23	0		281.81	0.19	0.10	2.54	14.94	17.19	0.78	'2'	922.6371	'1'	33.85
2003_26	1/21/03 0:00	35.99	-120.67		385.44	0		283.13	0.17	0.06	1.48	15.03	16.10	1.80	'2'	573.1996	'1'	32.53
2003_28	1/21/03 0:00	41.14	-124.11		955.67	0		284.81	0.25	0.28	3.59	33.09	30.41	2.70	'1'	117.8349	'1'	89.66

2003_29	1/21/03 0:00	34.67	-118.98		384.56	0		279.49	0.39	0.03	2.20	11.16	13.55	8.35	'4'	1820.822	'1'	41.30

Statistical Machine Learning Models

We use neural network and random forest machine learning models to quantify the relationship between our predictor variables and the risk of extreme growth. We also include simpler logistic regressing models.

Neural Network Models

We use a feed-forward, fully connected, shallow neural networks produced with the function "fitcnet" built into Matlab (https://www.mathworks.com/help/stats/fitcnet.html).

The output from the neural network is a classification score computed using the softmax activation function that follows the final fully connected layer in the network,

$$f(x_i) = \frac{e^{x_i}}{\sum_{j=1}^{2} e^{x_j}}. \qquad \text{S11}$$

Since we treat this as a binomial classification problem, the final fully connected layer has two outputs, x_1 and x_2. The scores output from the above equation can be interpreted as the posterior probabilities of extreme daily growth on that day, given an active fire and given the values of the features fed into the neural network.

Random Forest Model

We use a bootstrap aggregated (bagged) forest of decision trees produced with the function "treebagger" built into Matlab (https://www.mathworks.com/help/stats/treebagger.html).

The probability of observing extreme daily growth is taken as the fractional number of extreme daily growth days in a tree leaf from the training dataset averaged over all the trees in the ensemble (100 trees per model).

Logistic Regression Models

In addition to the neural network and random forest models, we use a logistic regression model produced with the Matlab function "fitglm" (https://www.mathworks.com/help/stats/fitglm.html). We make use of the function to create derived predictors that are non-linear and/or combinations of multiple predictors. Below are the four separate logistic regression models that result as well as their functional forms.

<u>Linear:</u> The model contains an intercept and linear term for each predictor.

$$p(y_i) = \frac{1}{1+e^{(-b_0-b_1x_1-\cdots)}} \qquad \text{S12}$$

<u>Pure Quadratic:</u> The model contains an intercept term and linear and squared terms for each predictor.

$$p(y_i) = \frac{1}{1+e^{(-b_0-b_1x_1-b_2x_1^2\dots)}} \qquad \text{S13}$$

<u>Interactions:</u> The model contains an intercept, linear term for each predictor, and all products of pairs of distinct predictors (no squared terms).

$$p(y_i) = \frac{1}{1+e^{(-b_0-b_1x_1-b_2x_1\cdot x_2-b_3x_1\cdot x_3\dots)}} \qquad \text{S14}$$

<u>Quadratic:</u> The model contains an intercept term, linear and squared terms for each predictor, and all products of pairs of distinct predictors.

$$p(y_i) = \frac{1}{1+e^{(-b_0 - b_1 x_1 - b_1 x_1^2 - b_2 x_1 \cdot x_2 - b_3 x_1 \cdot x_3 \ldots)}} \quad \text{S15}$$

where (x_1, x_2, …x_{11}) are the feature variables, and the model learns the coefficients b_0, b_1, …b_{11} to predict the probability of extreme growth $p(y_i)$

Varying Neural Network and Random Forest Hyperparameters

In order to identify the most reliable model types and hyperparameter configurations, we created an ensemble of 1,000 neural network and 1,000 random forest models (See supplementary dataset for all 2,000 configurations).

The neural networks varied in i) the number of layers in the network, ii) the number of neurons in each layer, iii) the activation functions for the fully connected layers, and the iv) value of a regularization term that penalizes large weights in the neural network by adding a ridge (L2) penalty term to the cost function. The random forest models varied in i) their minimum leaf size, ii) the maximum number of splits, and iii) the split criteria (either deviance or Gini's diversity index).

Random samples of these hyperparameters were generated with a "random search" function built into Matlab.

Machine Learning Model Performance and Relationship Between Performance and Calculated Shifts in Risk

We used four scoring methods to assess the performance of the 2,004 models (1,000 neural network, 1,000 random forest, and 4 logistic regression). These scoring methods were the log-loss score, the Brier Score, a Reliability Diagram Score, and an area under the Receiver Operating Characteristic curve, ROC-AUC. Ultimately, we use the log-loss score as our authoritative measure of model performance as it is the only scoring metric that satisfies the desirable conditions of additivity, "locality", and strictly proper behavior (*44*). However, we show results for the other three scores to assess the sensitivity of results to the chosen performance metric.

Leave-3-years-out cross-validation was used where predictions were made on one 3-year block of data at a time, using the remaining data to train the models (see video explanation of method: https://youtu.be/lHztGWzghRI

Log Loss (Binary Cross-Entropy) Skill Score.

The log-loss score is calculated as,

$$Log\ loss\ score = -\frac{1}{N}\sum_{i=1}^{N}\left(y_i \cdot log\big(p(y_i)\big) + (1-y_i)\cdot log\ (1-p(y_i)\big)\right). \quad \text{S16}$$

Above, y_i is the binary indicator (1=extreme growth, 0=not extreme growth), and $p(y_i)$ is the model's predicted probability of extreme growth. A perfect model has a log loss score of zero.

Brier Score

The Brier Score (*45*) is analogous to the mean square error and is calculated as,

$$Brier\ score = \frac{1}{N}\sum_{i=1}^{N}(p(y_i) - y_i)^2. \quad \text{S17}$$

A perfect model has a log loss score of zero.

Reliability Diagram Score

We measure how well-calibrated the models' predictions are using reliability diagrams (Fig. S3C, S3D) and a reliability diagram score. We use bin widths that vary such that the number of fire-days within each bin is constant. This number was 1,000 for the leave-3-years-out cross-validated data (Fig. S3C) and 300 for the Train on Cool, Test on Warm Experiment (Fig. S3D, see below). We calculate the reliability diagram score as the mean absolute error over all bins between the mean model-predicted probability of extreme growth within a bin and the actual observed frequency of extreme growth corresponding to those predictions. This is effectively the distance of the reliability diagram lines from the 1:1 line (Fig. S3C, S3D)

ROC-AUC

The Receiver Operating Characteristic Curve plots the true positive rate against the false-positive rate when continuously changing probability thresholds for a positive prediction. The area under this curve is a measure of model performance, with 1 being a perfect model and 0.5 representing a model with no discriminatory capacity. The ROC-AUC is calculated with the built-in Matlab function perfcurve (https://www.mathworks.com/help/stats/perfcurve.html).

Skill Scores

In Fig S3A and Fig. S3B, we convert raw log-loss, Brier, and reliability diagram scores into skill scores to make them more interpretable,

$$Skill\ Score = 1 - \frac{Score_{machine\ learning\ model}}{Score_{naive\ model}}. \qquad \text{S18}$$

The skill score we use compares the models’ scores to a score that would have been achieved if the baseline probability of extreme growth was predicted for every instance (the naïve model). Skill scores greater than 0 indicate that the machine learning model is performing better than the naïve model, and thus the predictors do indeed provide information on the risk of extreme daily growth. As the machine learning model approaches perfection, the skill score approaches 1. Since the ROC-AUC score is already normalized and ranges from 0.5 to 1, we leave that score as a raw score and do not convert it to a skill score.

Representative ensemble of machine learning models used for main reported results.

To make inferences about how the risk of extreme daily growth may change in the future, we wish to identify the model hyperparameter configurations that best generalize to out-of-sample data. Simultaneously, we are interested in the relationship between model-calculated change in risk and model preference on out of sample data. This information is shown in Fig. S3. Specifically, the leave-three-years out cross-validated skill of the 2,005 models (using the four different skill metrics) compared to their mean probability ratio (historical vs. preindustrial) over all fire-days is shown in Fig. S3A. Fig. S3B shows the same, but for the mean fraction of attributable risk. Mean probability ratios and fractions of attributable risk are not particularly sensitive to restricting models to higher standards of skill (i.e., they remain relatively stable when the top 2/3^{rds}, 1/3^{rd,} and 1/10th of model configurations are sampled.

We average over the top 10% of model configurations according to the log-loss skill score in our main reported results (black dots in all panels in Fig. S3A and S3B). In other words, once the top 10% of model configurations are identified, in terms of their log-loss score on out-of-sample data, their predicted probabilities for each fire day are averaged together prior to subsequent calculations of the probability ratios. The reasoning is that the model configurations that best predicted out-of-sample extreme growth days should also be the model configurations that we have the most confidence in for assessing shifts in probabilities of extreme growth with shifts in temperature. We also take these model configurations and conduct a Train on Cool, Test on Warm experiment (see below) that is analogous to the out-of-parameter space predictions being made under the climatological temperature changes being considered here.

Coincidentally, the top 10% of models (in terms of log-loss skill score) were equally represented by random forests and neural networks (50%-50% split). None of the four logistic regression models were in the top 10%.

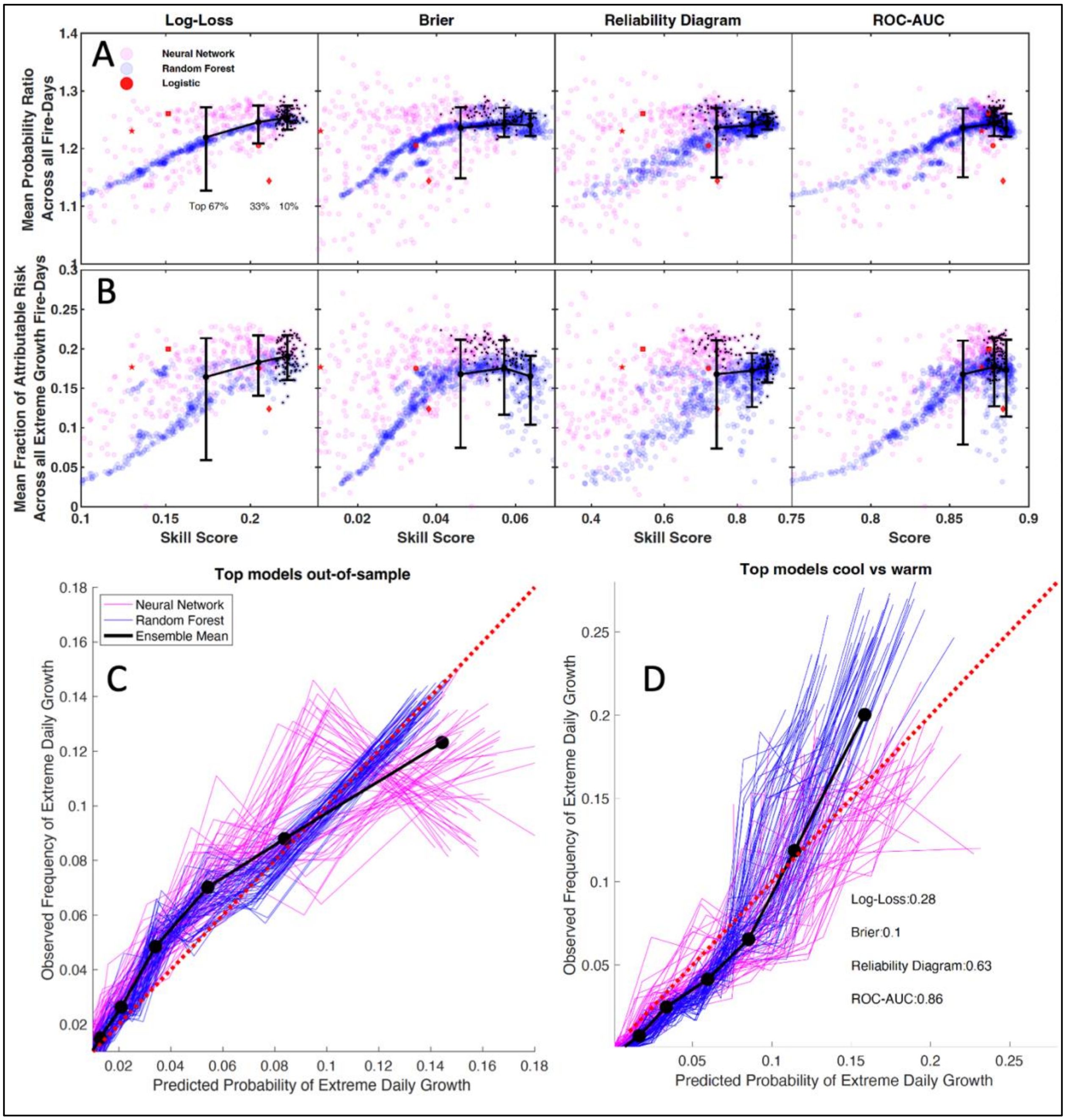

Fig. S3. (A) Relationship between a machine learning models' mean shift in probability (present vs. preindustrial, Y axis) across all fire-days and their out-of-training-sample performance using four score metrics (X axis) across 1,000 variations of neural network (magenta dots) and 1,000 variations of random forest (blue dots) hyperparameter combinations. There are also four versions of logistic regression models represented in red (The red circle corresponds to the Eq. S1, the red square corresponds to Eq. S2, the red diamond corresponds to eq. S3, and the red star corresponds to Eq. S4. The mean values across the top 2/3rds, 1/3rd, and 1/10th of models are shown with error bars of 5-95 percentile ranges. Results from the top 10% of models in the log-loss score (small black dots) are averaged together to produce all the main reported results of this study. (B) Same as (A) but for the Fraction of Attributable Risk of the extreme growth days. (C) Reliability diagrams for the top 10% of models (in terms of log-loss) using the leave-3-years out cross-validation. (D) same as (C) but using the train-on-cool, test on warm training-testing split experiment.

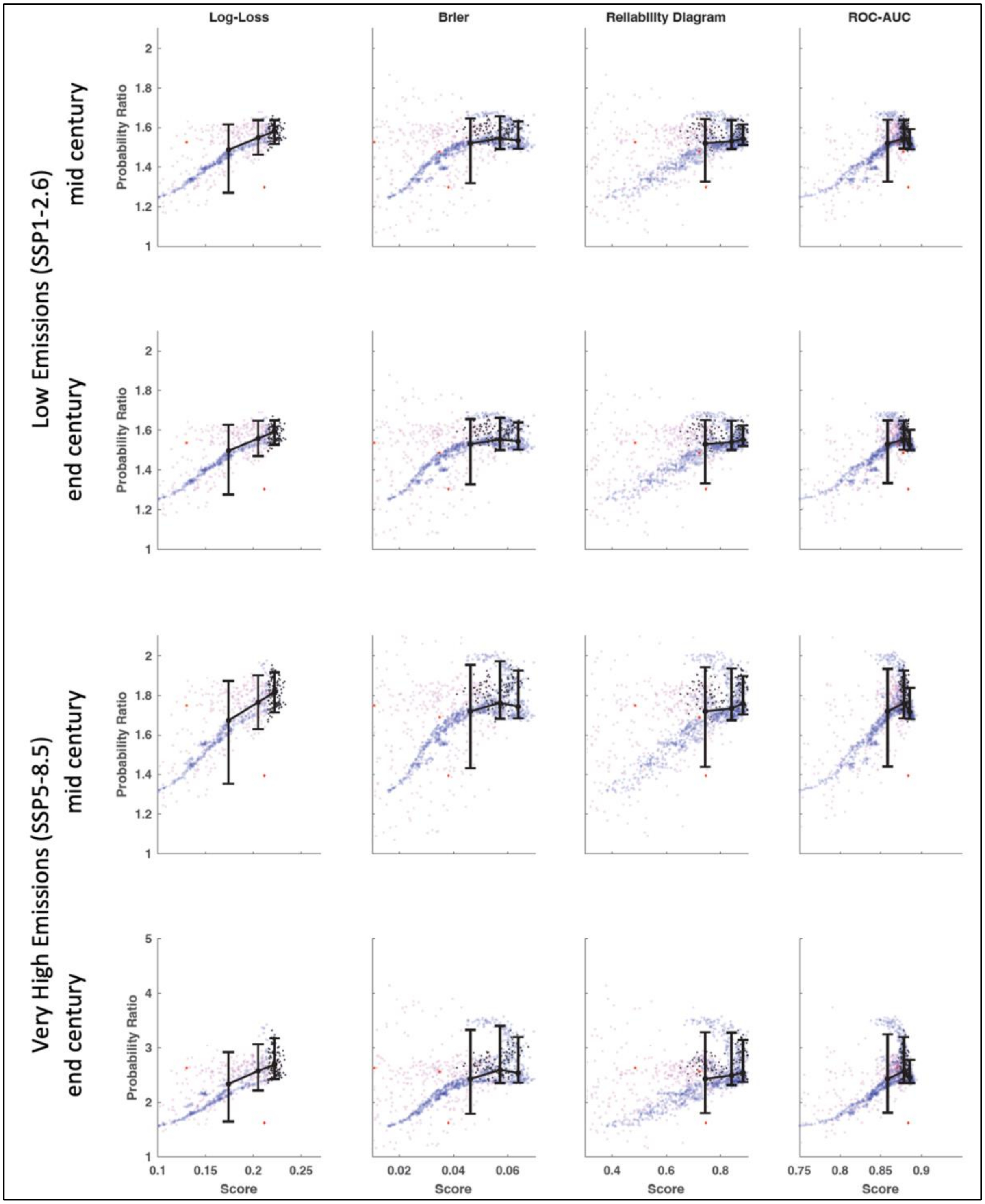

Fig. S4. Same as Fig. S3A but for future projected temperature changes.

Train on Cool, Test on Warm Experiment

Because of their large number of degrees of freedom, machine learning models are prone to overfitting and should always be tested on data that they are not trained on. Our main test of model performance is on out-of-sample data *in time* (using leave-3-years-out cross-validation, https://youtu.be/lHztGWzghRI?t=135). This out-of-sample test is important for a model to perform well on, however, an even more stringent test is one that assess the models' ability to make predictions on fire-days with novel predictors values (i.e., outside of the "parameter space" they were trained on). Since the point of this study is to compare predicted probabilities between current climates and future novel climates, it is relevant to demonstrate that the models can generalize and make reasonable predictions to this new parameter space.

In this "Train on Cool, Test on Warm Experiment", we divide the data such that the training-testing split separates the data in parameter space in a similar way to how the data is separated in parameter space between the historical and end-century SSP5-8.5 climates (the most extreme climate change scenario we consider). We then assess how well the pre-selected models that performed best on the cross-validation *in time* (black dots in Fig. S3A and S3B) performed making predictions using this new training testing split.

The distributions of predictor values across all fire-days between the historical climate and the end-century SSP5-8.5 climate are shown in the top row of Fig. S5.

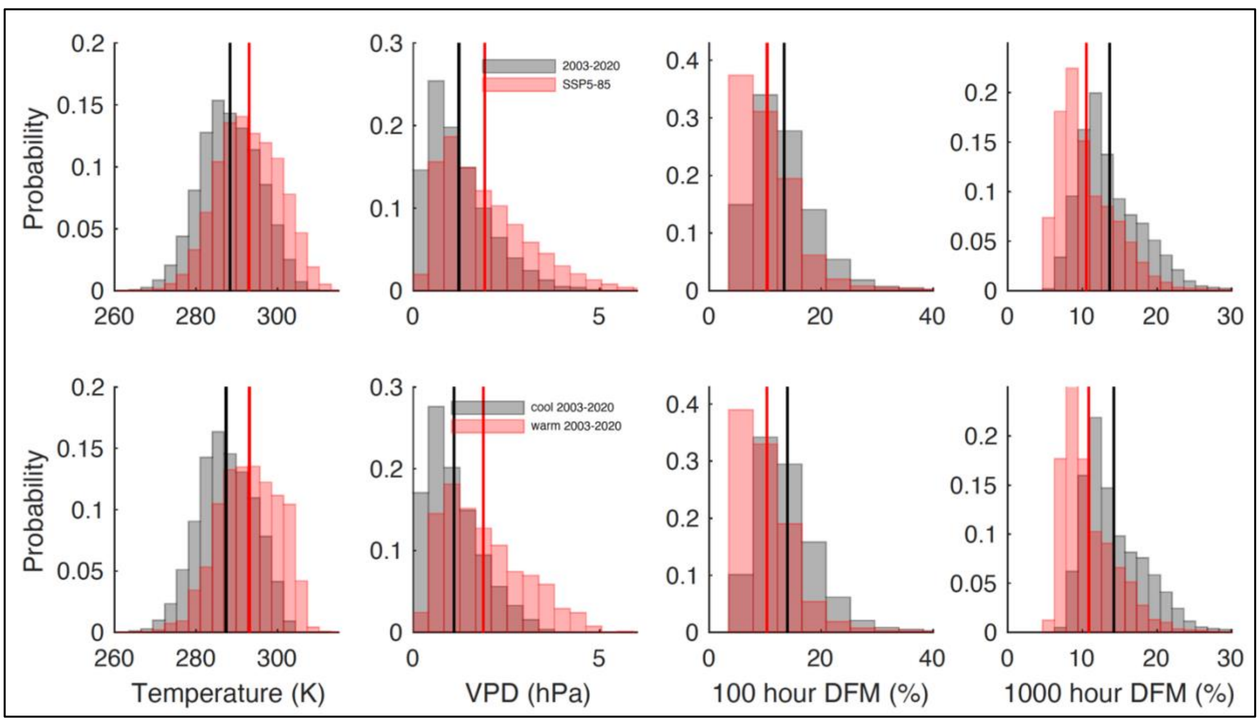

Fig. S5. Top) Distributions of predictor values (for the four that are altered) across all fire-days for the historical climate (grey) and end-century SSP5-8.5 (red). Bottom) Distributions of predictor values for the cool (grey) and warm (red) observations training/testing split. All distributions are normalized to sum to 1.

In order to split the data in a way that is analogous to the distributional differences in the top row of Fig. S5 (while attempting to preserve as many moments of the distributions as possible), we use a nearest-neighbor approach described below. There are four predictors that are shifted with climate change, but we illustrate the method using only two: temperature and 1000-hr dead fuel moisture (Fig. S6).

1. We begin with all 17,910 fire-days (black dots in Fig. S6)
2. We alter all predictor values in accordance with the climate change estimates for SSP5-8.5 (magenta dots in Fig. S6)
3. We select a random sample of 3,000 of these altered values (blue dots in Fig. S6), so we are left with the original 17,910 fire-days and 3,000 fire-days from the altered distribution.
4. We go through each of the 3,000 altered fire-days (blue) and find the fire-day from the original non-altered dataset (black) that is closest to it in parameter space. To find the closest fire-day in parameter space, we normalize all four predictors such that the minimum is zero and the maximum is one. We then find the minimal Pythagorean distance in four-dimensional space. Fire-days from the original dataset are only eligible to be picked once.

This procedure results in the selection of 3,000 fire-days from the original non-altered distribution that are the closest analogs to the 3,000 climate-change altered fire-days (red dots in Fig. S6). So we are left with 17,910-3,000=14,910 "cool" fire-days from the original dataset and 3,000 "warm" fire-days from the original dataset. The distributions of the four predictors for the "cool" and "warm" fire-days are shown in the bottom row of Fig. S5.

We then train the machine learning models on the cool fire-days and test them on the warm fire-days. The scores are shown in Fig. S3D. Of the four scoring metrics, the models performed better in two (log-loss and Brier) and worse in two (Reliability Diagram and ROC-AUC) than they did on the out-of-sample data in time.

In both model tests (out-of-sample in terms of time and out-of-sample in terms of parameter space), we interpret the results as indicating that the predictors do constrain the probability of extreme growth reasonably well, despite the models not having access to a great deal of relevant information (e.g., status of firefighting operations).

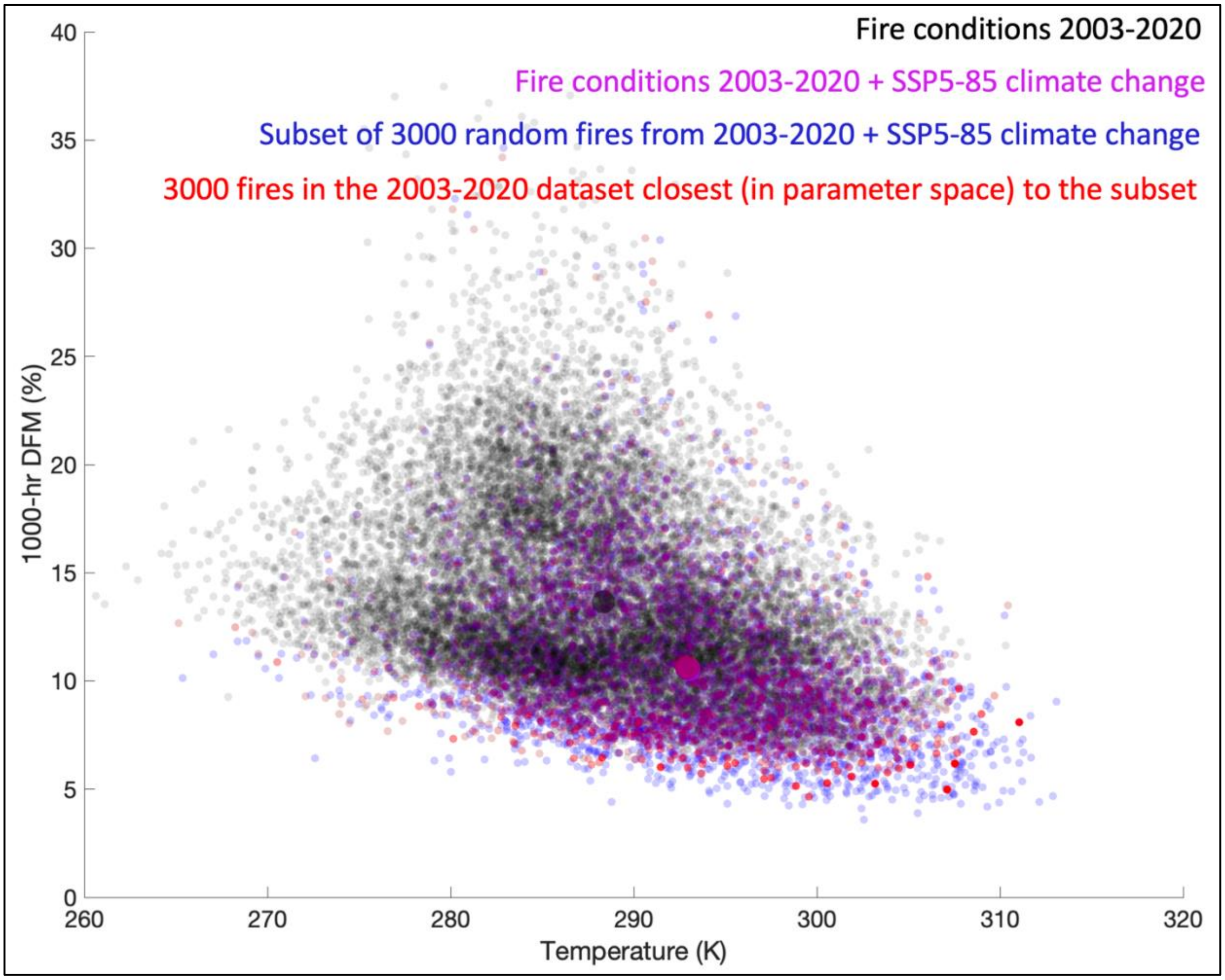

Fig. S6. Illustration of nearest neighbor approach in the train-on-cool, test-on-warm experiment. See text above for explanation.

Expected Frequency of Extreme Daily Growth

The machine learning models assign risk to days based purely on the environmental conditions on that day and contain no information on the antecedent behavior of the fire. Thus, the daily probabilities are not temporally dependent and would receive the same probabilities if their sequences were scrambled. This means that it is not unreasonable to treat the probabilities as being independent of each other and sum daily probabilities of extreme daily growth to get an estimate of the aggregate expected frequency of extreme daily growth. This is how the expected frequencies in Fig. 2G are calculated, with Poisson distributions used to estimate the expected random variability in these frequencies. The finding that the observed frequency of 380 falls reasonably within the Poisson distribution for the cross-validated historical predictions is evidence that summing the probabilities provides a reasonable estimate of aggregate expected frequency even if probabilities are not actually independent of each other.

For the notable destructive fires highlighted in Fig. 2A-F, and Fig. 3C, 3D, probability ratios are calculated across their lifetimes such that probabilities under a given climate condition are averaged before the ratio is taken,

$$Probability\ Ratio = \frac{\frac{1}{n}\sum_{i=1}^{n}(P(extreme\ growth \mid warmed\ T))_i}{\frac{1}{n}\sum_{i=1}^{n}(P(extreme\ growth \mid preindustrial\ T))_i}, \quad \text{S19}$$

where i represents a day in the lifetime of the fire and n is the total number of days.

Calculating the probability ratio this way allows it to be interpreted as the ratio in the expected frequency of extreme growth days across the lifetime of the fire. Using the same calculation across all fire-days results in ratios exactly proportional to the changes in expected aggregate frequency calculated in Fig. 2G. This is a different calculation than the mean probability ratio of the fire-days,

$$\frac{1}{n}\sum_{i=1}^{n}\left(\frac{P(extreme\ growth\mid warmed\ T)}{P(extreme\ growth\mid preindustrial\ T)}\right)_i, \qquad \text{S20}$$

which is what is displayed with vertical lines in the inset in Fig. 2.

Probability Ratios Below One

There are portions of the 11-dimensional parameter space where warming and drying (for vapor pressure deficit, 100 hour and 1,000 hour fuel moisture) results in a decrease in the probability of extreme daily growth and thus probability ratios below 1. Figure S7 compares the geographical occurrence and the historical predictor value distributions between fire-days that display probability ratios above 1 (95.4% of all fire-days, red) and fire-days that display a probability ratio below 1 (4.6% of all fire-days, blue). We speculate here on the possible causes of probability ratios below 1 but leave a detailed investigation to future work (likely requiring physical models to disentangle causality from association).

Fire-days with probability ratios below 1 are spread throughout the domain and not concentrated in any particular geographic location (Fig. S7). Their distributions are bimodal in temperature, vapor pressure deficit, dead fuel moisture, and vegetation fraction. There are local minimums in the occurrence of probability ratios below 1 near the critical thresholds identified in Fig. 3C and 3D.

The bimodal nature of the distributions of predictor values for fire-days with probability ratios below 1 suggests that at least two separate physical explanations might be necessary. Thus, figure S8 takes the fire-days with probability ratios below 1 and separates them by temperatures above and below 291K. This shows that these fire-days fit into two rough categories:

1) Those that are hot, dry, low elevation, low vegetation fraction, and disproportionately savanna/grassland (land classification 3)
2) Those that are cool, moist, higher elevation, high vegetation fraction, and disproportionately forest (land classification 1)

Category 1 fire-days seem to represent fires that are in fuel-limited, rather than aridity-limited conditions. Thus, in these situations, the machine learning models have associated increased temperature and aridity with decreased probability of extreme growth because this signals a move to a *more* arid situation that is likely *more* fuel-limited. Given that these are disproportionately savanna/grassland regions, it could indeed be the case that warming/drying (particularly in the 1,000 hour dead fuel moisture variable) reduces fuel loads and thus decreases the risk of extreme daily growth.

Category 2 fire-days are far on the moist side of the critical thresholds identified in Fig. 3C and 3D and thus not particularly prone to extreme daily growth. We speculate that in order to achieve extreme daily growth under these conditions, strong atmospheric instability must be present in order to generate a "plume-dominated" forest crown fires (*31*, *46*, *47*). However, warming and drying in these situations may be associated with higher lifting condensation levels and synoptic-scale high pressure, both of which would *increase* atmospheric stability, making plume aided spread less likely. This hypothesis can be tested in future work using dynamical fire-atmosphere coupled models (*48*).

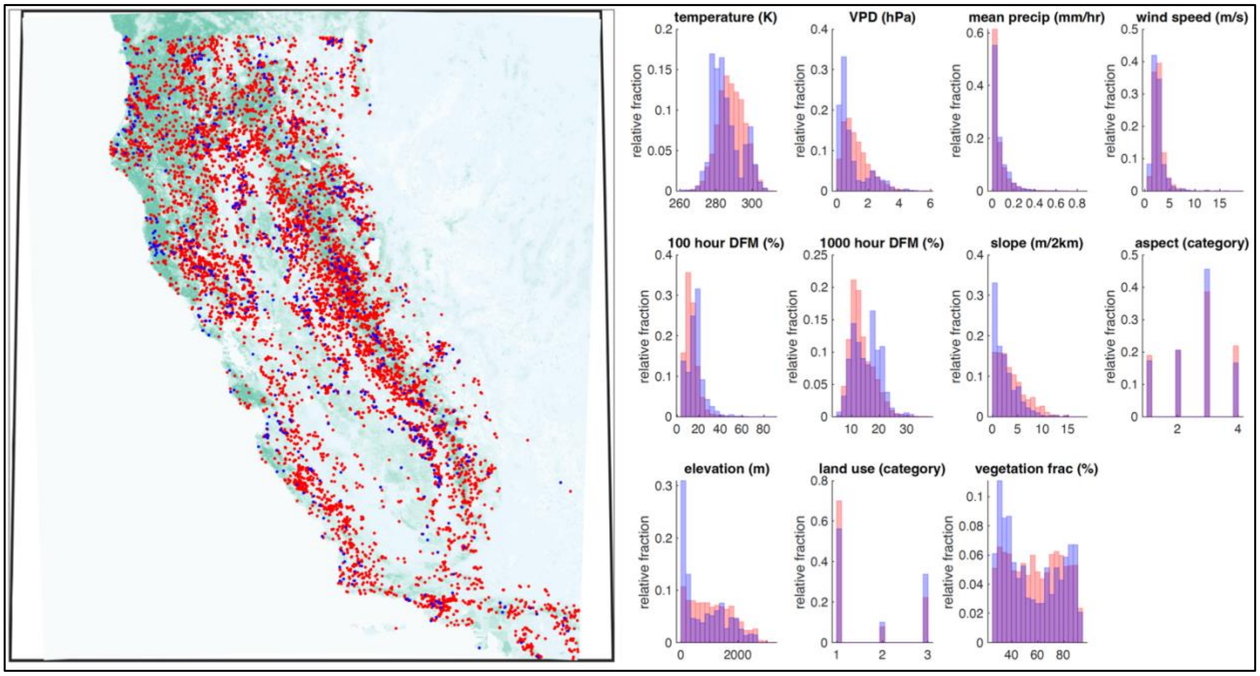

Fig. S7. Comparison of fire-days with historical vs. preindustrial probability ratios above 1 (red) and below 1 (blue).

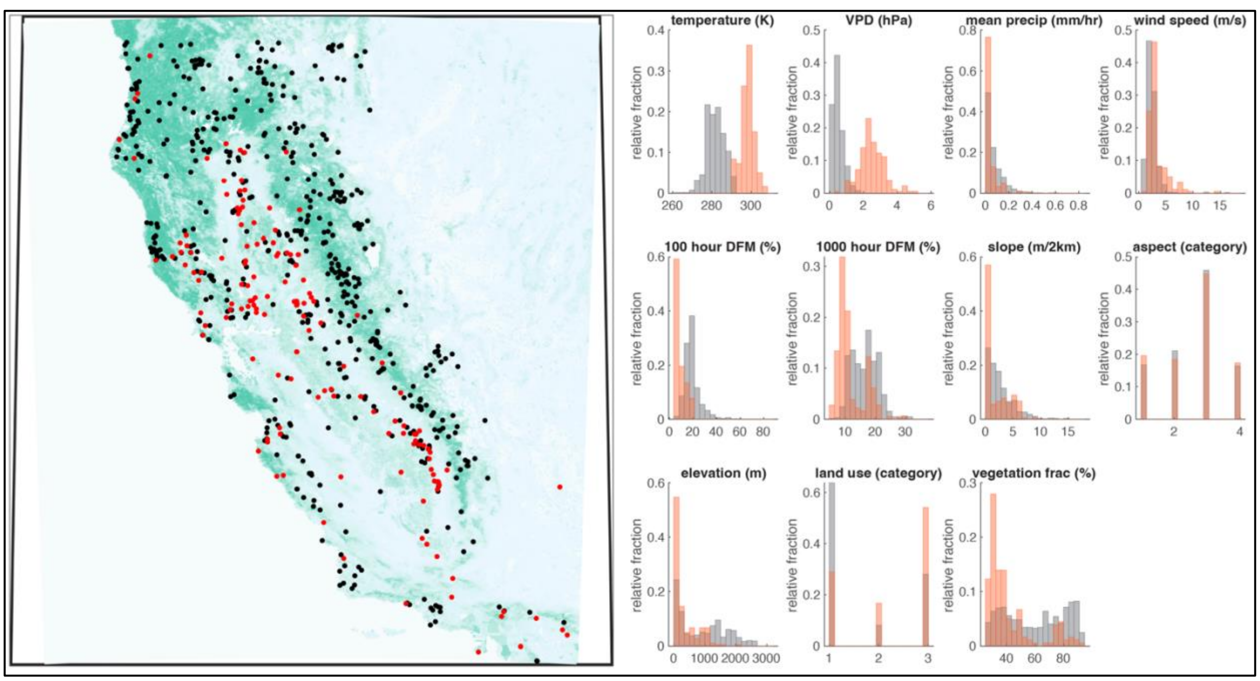

Fig. S8. The below 1 probability ratio fire-days from S7 split into categories of above 291 K (red) and below 291 K (black).

Other Supplementary Figures

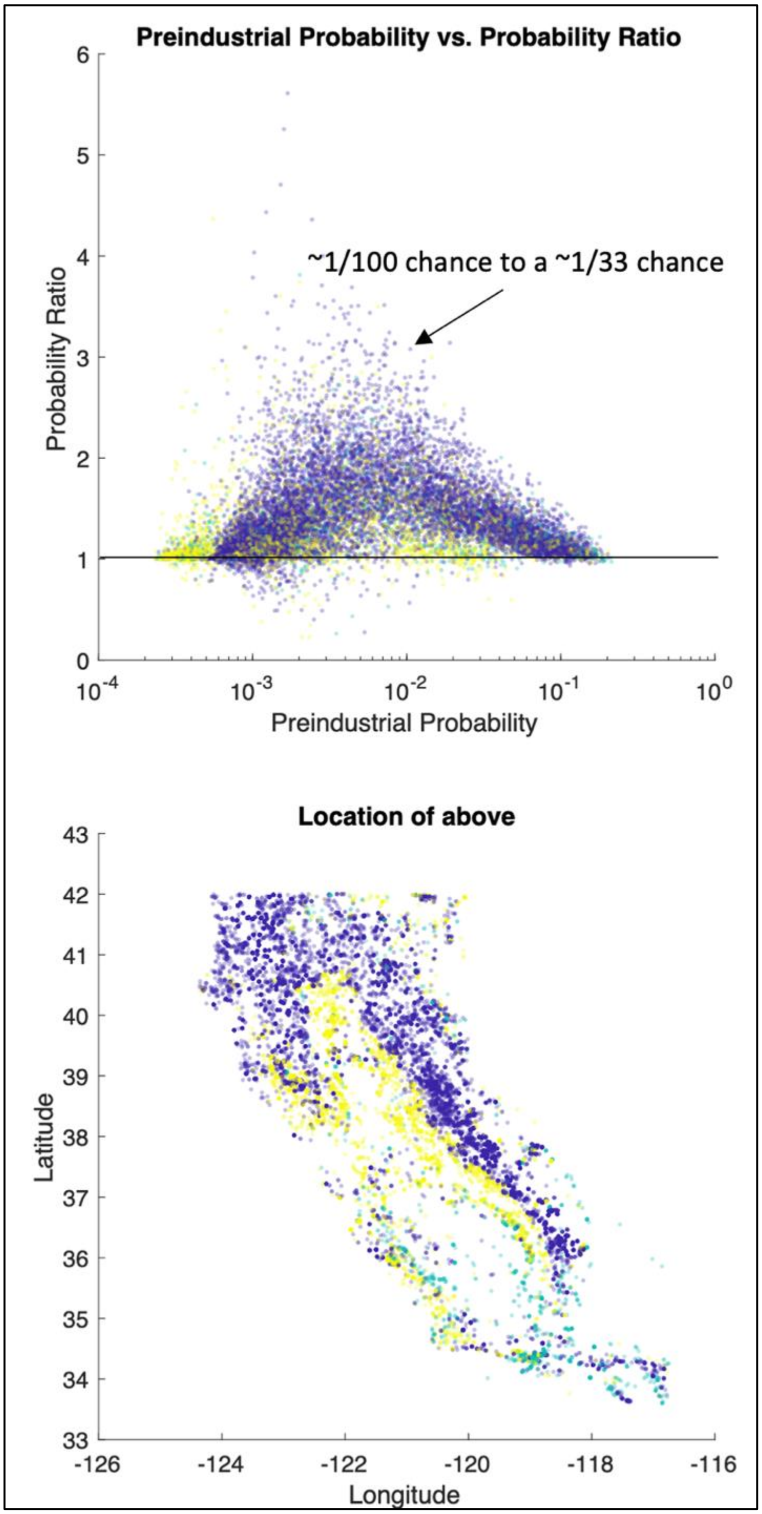

Fig. S9. Probability ratios as a function of preindustrial probability of extreme daily growth. The fire-days with the largest probability ratios tend to have preindustrial probabilities (of extreme daily growth) between 0.1% and 2%. This is roughly the probability of extreme growth for a fire-day just on the moist side of the identified critical thresholds (i.e., it is weather or aridity limited (*31*)), and thus anthropogenic warming causes large relative shifts in probability.

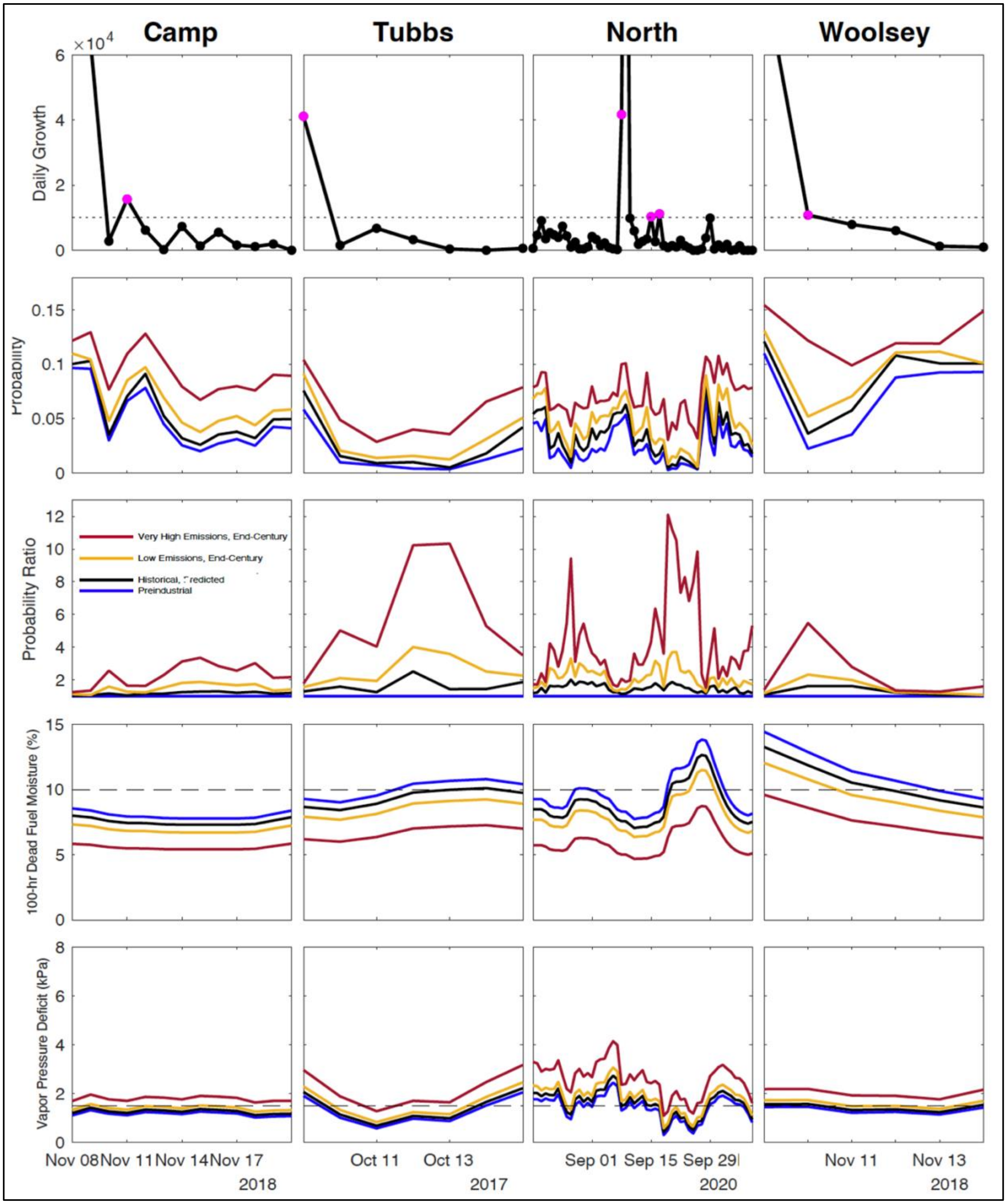

954 **Fig. S10. Same as Fig. 4 but for additional notable fires.**

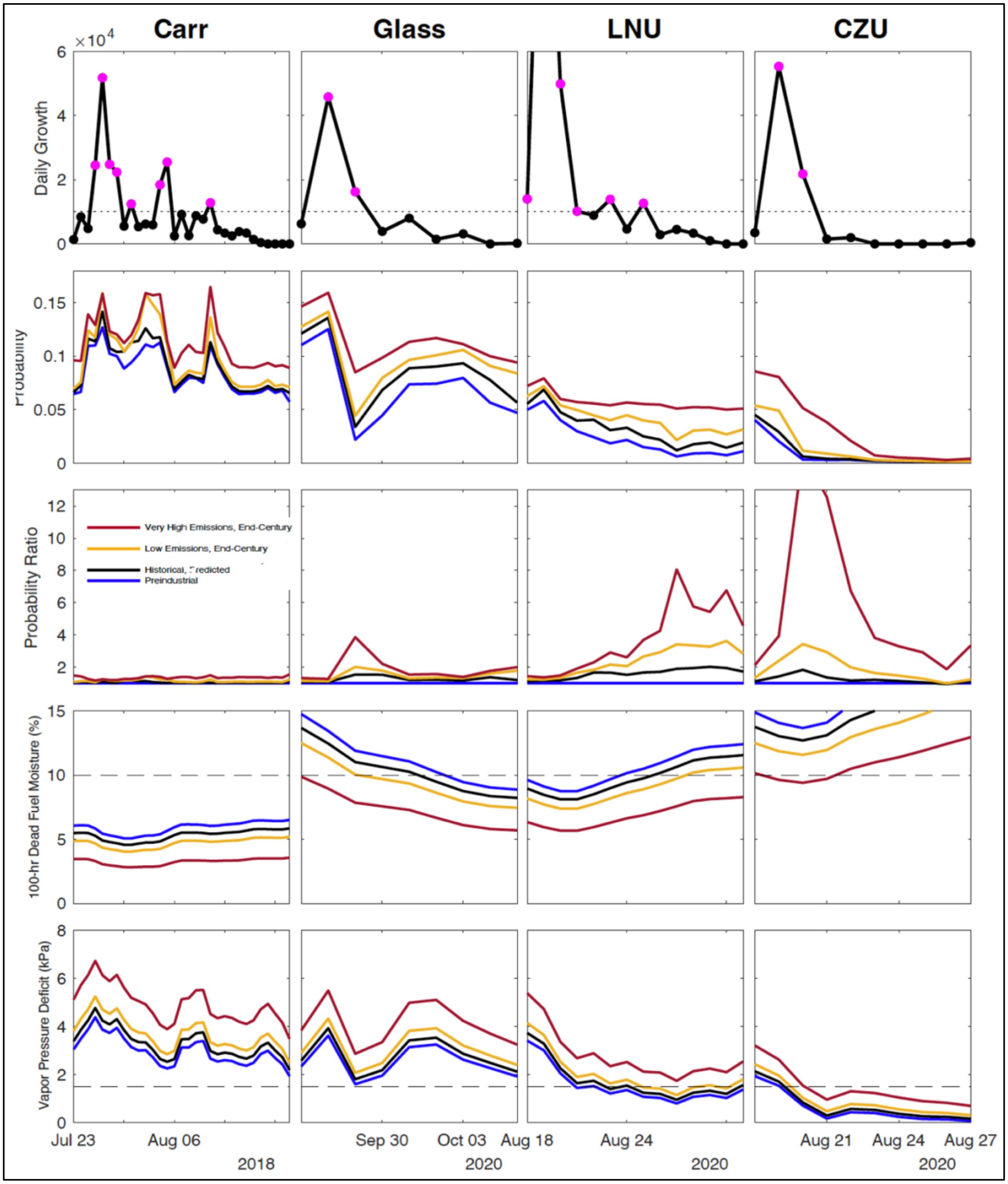

Fig. S11. Same as Fig. 4 but for additional notable fires.

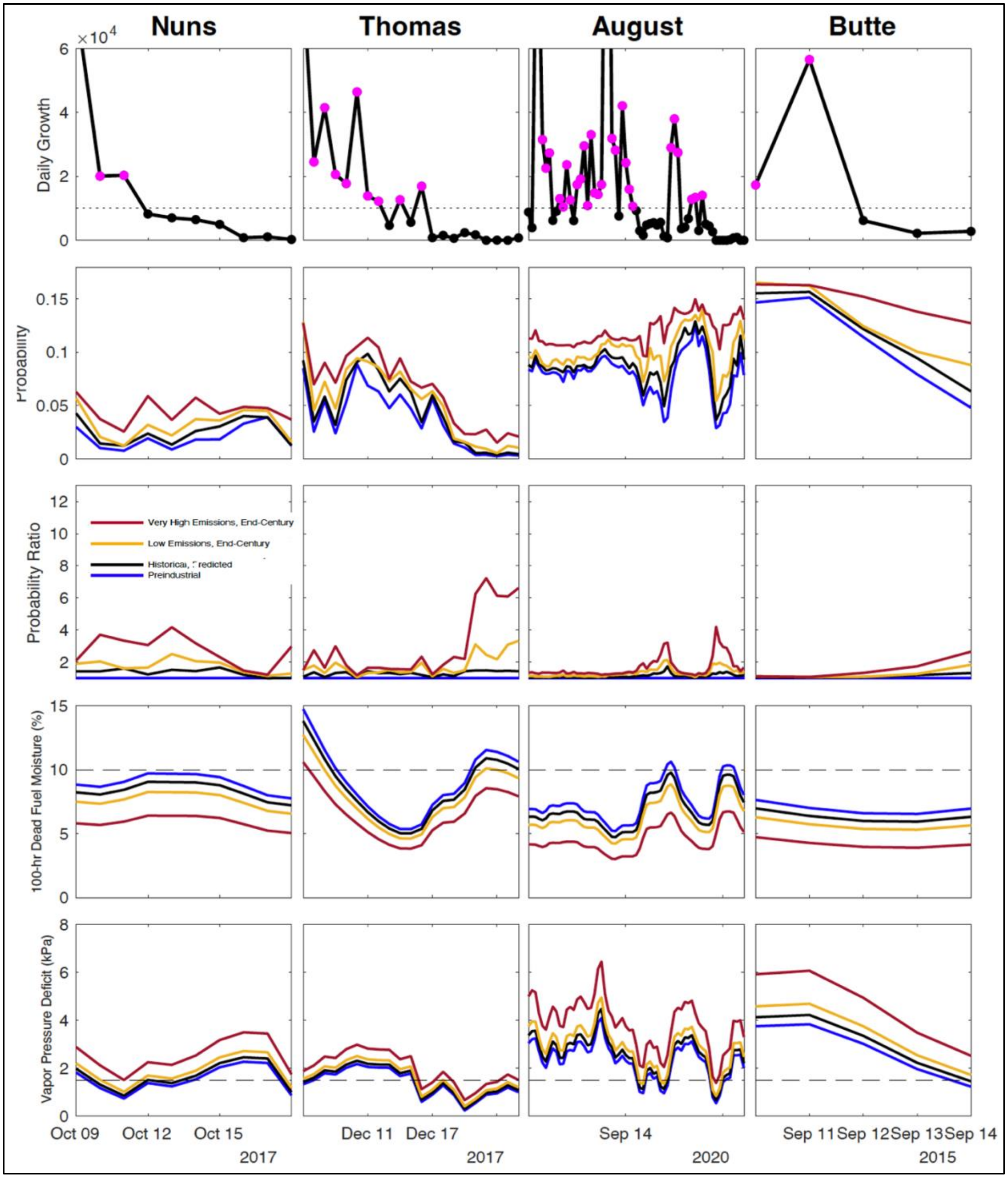

Fig. S12. Same as Fig. 4 but for additional notable fires.